

Emergent ferroelectricity in sub-nanometer binary oxide films on Si

Authors: Suraj S. Cheema^{1,2,*†}, Nirmaan Shanker^{2*}, Shang-Lin Hsu^{2*}, Yoonsoo Rho³, Cheng-Hsiang Hsu², Vladimir A. Stoica⁴, Zhan Zhang⁴, John W. Freeland⁴, Padraic Shafer⁵, Costas P. Grigoropoulos³, Jim Ciston⁶, Sayeef Salahuddin^{2,7†}

Affiliations:

¹Department of Materials Science and Engineering, University of California, Berkeley, CA, USA.

²Department of Electrical Engineering and Computer Sciences, University of California, Berkeley, CA, USA.

³Laser Thermal Laboratory, Department of Mechanical Engineering, University of California, Berkeley, CA, USA.

⁴Advanced Photon Source, Argonne National Laboratory, Lemont, IL, USA

⁵Advanced Light Source, Lawrence Berkeley National Laboratory, Berkeley, CA, USA.

⁶National Center for Electron Microscopy, Molecular Foundry, Lawrence Berkeley National Laboratory, Berkeley, CA, USA.

⁷Materials Sciences Division, Lawrence Berkeley National Laboratory, Berkeley, CA, USA.

*These authors contributed equally to this work

†Corresponding author. Email: s.cheema@berkeley.edu (SSC); sayeef@berkeley.edu (SS)

Abstract: The critical size limit of voltage-switchable electric dipoles has extensive implications for energy-efficient electronics, underlying the importance of ferroelectric order stabilized at reduced dimensionality. We report on the thickness-dependent antiferroelectric-to-ferroelectric phase transition in ZrO₂ thin films on silicon. The emergent ferroelectricity and hysteretic polarization switching in ultrathin ZrO₂, conventionally a paraelectric material, remarkably persists down to 5 Å thickness, the fluorite-structure unit cell size. This approach to exploit three-dimensional centrosymmetric materials deposited down to the two-dimensional thickness limit, particularly within this model fluorite-structure system possessing unconventional ferroelectric size effects, offers substantial promise for electronics, demonstrated by proof-of-principle atomic-scale nonvolatile ferroelectric memory on Si. Additionally, it is also indicative of hidden electronic phenomena achievable across a wide class of simple binary materials.

One-Sentence Summary: Ferroelectricity in conventionally-paraelectric ZrO₂ films is stabilized down to 5 Å thickness on Si via reduced dimensionality.

Main Text: The evolution of ferroic order at reduced dimensions, in particular two-dimensional (2D) ferroelectricity, has long been intriguing for scaled energy-efficient electronics (1) due to the inherent ability to control electric polarization with an applied voltage (2). Since the discovery of ferroelectricity and antiferroelectricity in HfO₂-ZrO₂-based thin films (3, 4), fluorite-structure binary oxides have reignited such interest (5) as they overcome many of the thickness scaling (6, 7) and silicon compatibility issues (8) afflicting its perovskite and vdW ferroelectric counterparts. Original studies into fluorite-structure systems examined the ferroelectric-antiferroelectric phase competition in HfO₂-ZrO₂ solid solutions as a function of composition (9), typically in the 10 nm regime (8); meanwhile, recent works demonstrated ferroelectricity down to sub-2-nm thickness in epitaxial (10) and polycrystalline (11) Zr:HfO₂ films.

Considering the implications of voltage-driven polarization switching for memory applications (8), the fundamental size limit of ferroelectric order in fluorite-structure systems is of critical importance. First-principles calculations have shown 2D HfO₂ layers in its polar orthorhombic structure (*Pca2*₁) have minimal electrostatic penalty, i.e. depolarizing field, enabling unsuppressed polarization down to the unit-cell (u.c.) limit (12, 13). Furthermore, monolayer ZrO₂ was predicted to support switchable polarization on an atomically abrupt structure with Si (14). These predictions of scale-free fluorite-structure ferroelectricity (12, 14) strongly motivate experimental demonstration of sub-nm polarization switching in this binary oxide system on silicon towards realizing highly-scaled low-power nonvolatile memories (8, 12).

Our strategy to achieve atomic-scale ferroelectricity aims to convert the conventionally antiferroelectric (AFE) tetragonal phase (t-phase) of ZrO₂ (t-ZrO₂: *P4*₂/*nmc*) to the ferroelectric (FE) orthorhombic phase (o-phase) of ZrO₂ (o-ZrO₂: *Pca2*₁) via reduced dimensionality (Fig. 1A). The reduced dimensionality stabilizes the pressure-induced ferroelectric o-phase in fluorite-based oxides – conventionally achieved via hydrostatic pressure (15), chemical pressure (9), or epitaxial strain (16) – in the ultrathin regime, akin to size-driven AFE-to-FE phase transitions observed in prototypical perovskite ferroelectrics (17). We demonstrate the emergence of atomic-scale ferroelectricity in conventionally-paraelectric ZrO₂ films down to 5 Å thickness, corresponding to the fluorite-structure unit-cell size.

ZrO₂ films from 10 nm down to 5 Å thickness (Fig. 1A), which we confirmed with synchrotron X-ray and TEM analysis (fig. S1, S2), are grown by atomic layer deposition (ALD) on SiO₂-buffered Si (Fig. 1C) (18). To study the thickness-dependent antiferroelectric-ferroelectric evolution in ZrO₂, we examined the structural signatures of the respective t- and o-phases (Fig. 1). Synchrotron in-plane grazing incidence diffraction (GID) spectra confirms the expected t-phase (101) reflection in thicker (3-10 nm) ZrO₂ films and the emergence of the o-phase (111) reflections for ultrathin (≤ 2 nm) films down to 5 Å thickness (Fig. 1B), concurrent with the emergence of highly-oriented films (fig. S3), and supported by detailed in-plane GID indexing (fig. S4) (18).

Distinguishing the nearly-identical polar o-phase and nonpolar t-phase structural polymorphs can be further clarified by local oxygen atomic imaging (19, 20). We used oxygen-sensitive negative spherical aberration imaging (NCSI) (20) and high-resolution transmission electron microscopy (HR-TEM) to identify the expected nonpolar t-phase in 5 nm ZrO₂ films (Fig. 1D,E), aided by oxygen analysis (fig. S5) and HR-TEM simulations (fig. S6). Notably, this technique indicates the polar o-phase emerges in 2 nm ZrO₂ films (Fig. 1F,G), which X-ray analysis (Fig. 1B) pinpoints as the onset of ferroelectric o-ZrO₂ stabilization, as identified by its characteristic zig-zag-like oxygen arrangement visible along the [110] projection (Fig. 1G). Additionally, lattice

angle analysis from traditional cation imaging matches $P4_2/nmc$ and $Pca2_1$ HR-TEM simulations for 5 nm and 2 nm ZrO_2 films, respectively (fig. S7), consistent with oxygen imaging.

To further examine this thickness-dependent AFE-to-FE transition, we employed additional synchrotron X-ray studies to detect structural signatures of the respective ferroic phases (Fig. 2). From thickness-dependent GID, we found that the interplanar lattice spacing (o - d_{111} or t - d_{101}) and aspect ratio ($2c/(a+b)$ or c/a), structural barometers of lattice distortion established for fluorite-structure films (18), sharply rise below 3 nm thickness (Fig. 2A). These observations indicate increased polar o - ZrO_2 stabilization in the atomic-scale limit (Fig. 1B). Along with diffraction, X-ray spectroscopy provides another gauge of the fluorite-structure symmetry. Thickness-dependent XAS spectra at the oxygen K -edge (fig. S8) demonstrate larger crystal field splitting (Fig. 2B) below 3 nm, suggesting more pronounced polar distortion (18). In fact, secondary crystal field splitting arising from the polar rhombic distortion, a fingerprint of the ferroelectric o -phase (fig. S8), emerges for 5 and 10 Å ZrO_2 . Furthermore, X-ray linear dichroism (XLD) from zirconium $M_{3,2}$ - and $L_{3,2}$ -edges (fig. S8) indicate more pronounced orbital polarization, linked to electric polarization arising from ferroelectric polar distortions (11, 18), in the ultrathin regime (Fig. 2B). These thickness-dependent diffraction and spectroscopy trends support the ultrathin-amplified emergence of FE o - ZrO_2 in typically AFE t - ZrO_2 films.

Optical microscopy observations also support the size-dependent ferroic phase evolution, as the increase in second harmonic generation (SHG) signal, which is related to macroscopic polarization (18), with decreasing ZrO_2 thickness (Fig. 2C) is consistent with the ultrathin-enhanced polar distortion trends. Additionally, thickness-dependent capacitance-voltage (C - V) measurements of metal-oxide-semiconductor capacitors (fig. S9) indicate a crossover from antiferroelectric-like t -phase permittivity (κ), $\kappa \sim 40$ (4), towards more ferroelectric-like o -phase permittivity, $\kappa \sim 30$ (4, 21), for ultrathin ZrO_2 films, again consistent with structural characterization.

To further characterize the electrical behavior, we fabricated metal-insulator-metal (MIM) capacitors with varying ZrO_2 thickness (Fig. 3A). Considering that antiferroelectrics are defined based on its field-induced transition to a proximal polar phase and not simply its parent crystal structure (17), voltage-dependent hysteretic behavior is required to probe the underlying ferroic order, beyond crystallographic signatures of its parent structure. MIM polarization-voltage (P - V) loops for 5 and 10 nm thick ZrO_2 , the typical t - ZrO_2 thickness regime (4, 8), demonstrate a signature antiferroelectric-like double hysteresis (17) (Fig. 3B). Importantly, conventional P - V probes of the signature behavior cannot be applied to the ultrathin regime (18), in which non-polarization-dependent leakage current masks polarization-dependent switching current.

To directly probe the polarization switching properties of ultrathin ZrO_2 films while suppressing leakage current, we fabricated interdigitated electrodes (IDE) to facilitate in-plane (IP) polarization switching (Fig. 3D). In IDE structures, leakage is no longer limited by the ZrO_2 thickness (~ 5 Å - 10 nm), but rather the in-plane electrode spacing (~ 1 μm). The expected field-induced nonpolar-to-polar phase transition for fluorite-structure antiferroelectrics (8, 18), illustrated by double-switching P - V behavior in the IDE structures, is observed for thick (5, 10 nm) t - ZrO_2 films (Fig. 3E, fig. S10). As ZrO_2 drops below the critical 2 nm thickness, P - V behavior for 1 nm and 5 Å ZrO_2 displays ferroelectric-like counterclockwise polarization switching (Fig. 3F, fig. S10). The polarization switching in this IP geometry is consistent with SHG imaging (Fig. 2C) and SHG spectra (fig. S11), whose geometry (fig. S12) is sensitive to IP inversion symmetry-breaking (18), rather than OOP inversion symmetry-breaking mapped by PFM imaging (fig. S13).

Pulsed I - V measurements in metal-ferroelectric-insulator-semiconductor (MFIS) tunnel junction structures (Fig. 3C) provide additional ferroic phase insights into ZrO_2 , in which tunnel electroresistance (TER) reflects the ferroelectric polarization evolution with field (18). For ultrathin (1 nm and 0.5 nm) ZrO_2 tunnel barriers (Fig. 3C), abrupt bistable resistance states exhibit counterclockwise hysteresis, consistent with ferroelectric polarization switching in the MFIS geometry and voltage-polarity independent hysteretic behavior (fig. S14). Similar TER hysteresis maps have been shown for FTJs integrating ultrathin Zr:HfO₂ barriers (11, 22, 23), but until this point, fluorite-based FTJs have not been demonstrated below 1 nm.

To unravel these anomalous size effects, specifically the emergent 2D ferroelectricity in a conventionally paraelectric material, surface energies, which take on an amplified role in the ultrasmall and ultrathin regime (21), can provide key insights into fluorite polymorphic phase stability (15). First-principles calculations considering surface energy contributions predict lower o-phase Gibbs free energy relative to the t-phase at ultrasmall sizes (< 4 nm) and large pressures for the HfO₂-ZrO₂ system (21). Indeed, pressure-driven stabilization of the o-phase in ZrO_2 has been observed via hydrostatic pressure in bulk ZrO_2 (15) and epitaxial strain in thin film ZrO_2 (16, 24). Here, 2D thickness-scaling, i.e. confinement in the vertical dimension (Fig. 1A), should trigger similar pressure-driven and surface-energy-induced effects. Accordingly, the FE o-phase is stabilized at reduced dimensions, as expected for ultrasmall crystallite sizes (20) and nanoscale grain sizes (21) in fluorite binary oxides. On the other hand, similar size effects typically destabilize the polar crystal structure in the conventional perovskite ferroelectrics (25), marking one key distinction between the two ferroelectric systems.

Besides simply stabilizing atomic-scale ferroelectricity, another puzzling feature lies in the amplified markers of polar distortion with decreased thickness (Fig. 2). In fact, ZrO_2 demonstrates many of the same ultrathin-enhanced lattice distortion signatures as ferroelectric polycrystalline Zr:HfO₂ (11) and epitaxial Zr:HfO₂ (10, 26) films. Therefore, these "reverse" size effects relative to its perovskite counterparts, in which polarization typically decreases with decreasing thickness (7), may be intrinsic to fluorites. Recent first-principles calculations indicate that the fluorite-structure o-phase ($Pca2_1$) displays a negative longitudinal piezoelectric effect (NLPE) (27), in which compression along the polarization direction leads to a larger polar distortion. Therefore, the NLPE could provide an atomic-scale mechanism underlying the observed increased polar distortion as thickness is reduced to the ultrathin regime (10, 11, 26) in fluorite-structure ferroelectrics. This would mark another distinguishing feature from prototypical perovskite-based ferroelectric thin films, which demonstrate positive longitudinal piezoelectricity and diminished polar distortion at the atomic-scale (7).

Along with the distinct piezoelectric origins (27), unconventional ferroelectric origins have also been attributed to fluorite-structure binary oxides (12, 13). First-principles calculations suggest 2D fluorite-structure $Pca2_1$ slabs maintain switchable polarization due to its improper nature (12); indeed, for improper ferroelectric transitions, the primary nonpolar structural distortion, from which the spontaneous polarization indirectly arises, is impervious to electrostatic depolarization effects (28). Therefore, improper fluorite ferroelectrics should display robust, switchable electric dipoles with no critical thickness (12), as we observed for ultrathin ZrO_2 (Fig. 3).

In addition to the depolarization-resistant nature of fluorite ferroelectricity (12, 13), in-plane (IP) polarization can also help mitigate depolarization fields, which typically suppress out-of-plane (OOP) polarization in the ultrathin regime (29). Indeed, the ultrathin o- ZrO_2 films demonstrate IP polarization, evidenced by IP inversion symmetry-breaking (Fig. 2C) and polarization switching

(Fig. 3F). These films exhibit predominant (111) OOP texture (Fig. 2A, fig. S3); considering the $Pca2_1$ unit cell polar axis lies along a principal lattice direction, o-ZrO₂ films project a substantial IP polarization. Therefore, the highly-oriented nature of the ultrathin ZrO₂ films, preferentially stacked along its close-packed (111) planes favored by surface energy considerations, can also contribute to the sustained atomic-scale polarization.

Considering traditional 3D materials may possess unrealized spontaneous polarization, exemplified here by a conventionally paraelectric binary oxide developing ferroelectric order at reduced dimensions, simply scaling the thickness to the atomic-scale offers a straightforward yet effective route to 2D ferroelectricity-by-design in intrinsically centrosymmetric materials.

Therefore, reduced dimensionality offers a powerful inversion-symmetry-breaking methodology (30), along with epitaxial strain (31, 32) and twisted heterostructures (33), for materials in proximity to pressure-induced polar instabilities, e.g. other simple binary oxides (34).

Specifically regarding the HfO₂-ZrO₂ binary oxide family, the emergence of atomic-scale ferroelectricity in ZrO₂ underscores the distinct nature of fluorite-structure size effects, in which reduced dimensionality induces ferroelectric order even in its conventionally antiferroelectric endmember, not just Zr:HfO₂ (11). Therefore, thickness-scaling alone can span the fluorite ferroelectric-antiferroelectric phase diagram, moving beyond the established HfO₂-ZrO₂ composition space (4, 8, 9). Furthermore, the observed polarization switching (Fig. 3) to the fluorite-structure unit cell size, 5 Å, validates recent predictions of its unorthodox ferroelectric origins (12, 13), likely marking the thinnest demonstration of hysteretic polarization switching in any ferroelectric system (table S1). Critically, the polarization switching for 5 Å ZrO₂ persists beyond 125°C (fig. S15), promising for electronic applications, e.g. nonvolatile ferroelectric memory (Fig. 3C). Therefore, simple fluorite-structure binary oxides offer a model material system not just to explore unconventional piezoelectric and ferroelectric phenomena at the 2D limit, but also for integration into highly-scaled next-generation Si electronics.

References and Notes

1. S. Salahuddin, K. Ni, S. Datta. The era of hyper-scaling in electronics. *Nature Electronics* **1**, 442–450 (2018).
2. M. Dawber, K. M. Rabe, J. F. Scott. Physics of thin-film ferroelectric oxides. *Review of Modern Physics* **77**, 1083–1130 (2005).
3. T. S. Böske, J. Müller, D. Bräuhaus, U. Schröder, U. Böttger. Ferroelectricity in hafnium oxide thin films. *Applied Physics Letters* **99**, 102903 (2011).
4. J. Müller, T. S. Böske, U. Schröder, S. Mueller, D. Bräuhaus, U. Böttger, L. Frey, T. Mikolajick. Ferroelectricity in Simple Binary ZrO₂ and HfO₂. *Nano Letters* **12**, 4318–4323 (2012).
5. T. Mikolajick, U. Schroeder, M. H. Park. Special topic on ferroelectricity in hafnium oxide: Materials and devices. *Applied Physics Letters* **118**, 180402 (2021).
6. H. Qiao, C. Wang, W. S. Choi, M. H. Park, Y. Kim. Ultra-thin ferroelectrics. *Materials Science and Engineering: R: Reports* **145**, 100622 (2021).

7. J. F. Ihlefeld, D. T. Harris, R. Keech, J. L. Jones, J. Maria, T. Susan. Scaling Effects in Perovskite Ferroelectrics: Fundamental Limits and Process-Structure-Property Relations. *Journal of the American Ceramic Society* **99**, 2537–2557 (2016).
- 5 8. T. Mikolajick, S. Slesazeck, H. Mulaosmanovic, M. H. Park, S. Fichtner, P. D. Lomenzo, M. Hoffmann, U. Schroeder. Next generation ferroelectric materials for semiconductor process integration and their applications. *Journal of Applied Physics* **129**, 100901 (2021).
9. U. Schroeder, M. Materano, T. Mittmann, P. D. Lomenzo, T. Mikolajick, A. Toriumi. Recent progress for obtaining the ferroelectric phase in hafnium oxide based films: impact of oxygen and zirconium. *Japanese Journal of Applied Physics* **58**, SL0801 (2019).
- 10 10. Y. Wei, P. Nukala, M. Salverda, S. Matzen, H. J. Zhao, J. Momand, A. S. Everhardt, G. Agnus, G. R. Blake, P. Lecoer, B. J. Kooi, J. Íñiguez, B. Dkhil, B. Noheda. A rhombohedral ferroelectric phase in epitaxially strained $\text{Hf}_{0.5}\text{Zr}_{0.5}\text{O}_2$ thin films. *Nature Materials* **17**, 1095–1100 (2018).
- 15 11. S. S. Cheema, D. Kwon, N. Shanker, R. dos Reis, S.-L. Hsu, J. Xiao, H. Zhang, R. Wagner, A. Datar, M. R. McCarter, C. R. Serrao, A. K. Yadav, G. Karbasian, C.-H. Hsu, A. J. Tan, L.-C. Wang, V. Thakare, X. Zhang, A. Mehta, E. Karapetrova, R. V. Chopdekar, P. Shafer, E. Arenholz, C. Hu, R. Proksch, R. Ramesh, J. Ciston, S. Salahuddin. Enhanced ferroelectricity in ultrathin films grown directly on silicon. *Nature* **580**, 478–482 (2020).
- 20 12. H.-J. Lee, M. Lee, K. Lee, J. Jo, H. Yang, Y. Kim, S. C. Chae, U. Waghmare, J. H. Lee. Scale-free ferroelectricity induced by flat phonon bands in HfO_2 . *Science*, **369**, 1343–1347 (2020).
13. B. Noheda, J. Iniguez. A key piece of the ferroelectric hafnia puzzle. *Science*, **369**, 1300–1301 (2020).
- 25 14. M. Dogan, S. Fernandez-Peña, L. Kornblum, Y. Jia, D. P. Kumah, J. W. Reiner, Z. Krivokapic, A. M. Kolpak, S. Ismail-Beigi, C. H. Ahn, F. J. Walker. Single Atomic Layer Ferroelectric on Silicon. *Nano Letters* **18**, 241–246 (2018).
15. O. Ohtaka, H. Fukui, T. Kunisada, T. Fujisawa, K. Funakoshi, W. Utsumi, T. Irifune, K. Kuroda, T. Kikegawa. Phase relations and equations of state of ZrO_2 under high temperature and high pressure. *Physical Review B* **63**, 174108 (2001).
- 30 16. T. Song, H. Tan, N. Dix, R. Moalla, J. Lyu, G. Saint-Girons, R. Bachelet, F. Sánchez, I. Fina. Stabilization of the Ferroelectric Phase in Epitaxial $\text{Hf}_{1-x}\text{Zr}_x\text{O}_2$ Enabling Coexistence of Ferroelectric and Enhanced Piezoelectric Properties. *ACS Applied Electronic Materials* **3**, 2106–2113 (2021).
- 35 17. C. A. Randall, Z. Fan, I. Reaney, L. Chen, S. Trolier-McKinstry. Antiferroelectrics: History, Fundamentals, Crystal Chemistry, Crystal Structures, Size Effects, and Applications. *Journal of the American Ceramic Society* **104**, 3775–3810 (2021).

18. Materials, methods, and additional information are available as supplementary materials.
19. P. Nukala, M. Ahmadi, Y. Wei, S. de Graaf, S. Matzen, H. W. Zandbergen, B. Kooi, B. Noheda. Reversible oxygen migration and phase transitions in hafnia-based ferroelectric devices. *Science* **372**, 630–635 (2021).
- 5 20. H. Du, C. Groh, C.-L. Jia, T. Ohlerth, R. E. Dunin-Borkowski, U. Simon, J. Mayer. Multiple polarization orders in individual twinned colloidal nanocrystals of centrosymmetric HfO₂. *Matter* **4**, 986–1000 (2021).
- 10 21. R. Materlik, C. Künneth, A. Kersch. The origin of ferroelectricity in Hf_{1-x}Zr_xO₂: A computational investigation and a surface energy model. *Journal of Applied Physics* **117**, 134109 (2015).
22. Y. Wei, S. Matzen, T. Maroutian, G. Agnus, M. Salverda, P. Nukala, Q. Chen, J. Ye, Lecoeur, B. Noheda. Magnetic Tunnel Junctions Based on Ferroelectric Hf_{0.5}Zr_{0.5}O₂ Tunnel Barriers. *Physical Review Applied*, **12**(3),031001, (2019).
- 15 23. S. S. Cheema, N. Shanker, C.-H. Hsu, A. Datar, J. Bae, D. Kwon, S. Salahuddin. One Nanometer HfO₂-Based Ferroelectric Tunnel Junctions on Silicon. *Advanced Electronic Materials* 2100499 (2021).
24. S. E. Reyes-Lillo, K. F. Garrity, K. M. Rabe. Antiferroelectricity in thin-film ZrO₂ from first principles. *Physical Review B* **90**, 140103 (2014).
- 20 25. W. J. Merz. The effect of hydrostatic pressure on the curie point of barium titanate single crystals. *Physical Review* **77**, 52–54 (1950).
26. J. Lyu, I. Fina, R. Solanas, J. Fontcuberta, F. Sánchez. Growth Window of Ferroelectric Epitaxial Hf_{0.5}Zr_{0.5}O₂ Thin Films. *ACS Applied Electronic Materials* **1**, 220–228 (2019).
- 25 27. J. Liu, S. Liu, J.-Y. Yang, L. Liu. Electric Auxetic Effect in Piezoelectrics. *Physical Review Letters* **125**, 197601 (2020).
28. N. Sai, C. J. Fennie, A. A. Demkov. Absence of Critical Thickness in an Ultrathin Improper Ferroelectric Film. *Physical Review Letters* **102**,107601 (2009).
29. J. Junquera, P. Ghosez. Critical thickness for ferroelectricity in perovskite ultrathin films. *Nature* **422**, 506–509 (2003).
- 30 30. D. Lee, H. Lu, Y. Gu, S.-Y. Choi, S.-D. Li, S. Ryu, T. R. Paudel, K. Song, E. Mikheev, S. Lee, S. Stemmer, D. A. Tenne, S. H. Oh, E. Y. Tsybal, X. Wu, L.-Q. Chen, A. Gruverman, C. B. Eom. Emergence of room-temperature ferroelectricity at reduced dimensions. *Science* **349**, 1314–1317 (2015).

31. M. P. Warusawithana, C. Cen, C. Sleasman, J. Woicik, Y. Li, L. Kourkoutis, J. Klug, H. Li, P. Ryan, L. Wang, M. Bedzyk, D. Muller, L. Chen, J. Levy, D. Schlom. A ferroelectric oxide made directly on silicon. *Science* **324**, 367–370 (2009).
- 5 32. J. H. Haeni, P. Irvin, W. Chang, R. Uecker, P. Reiche, Y. L. Li, S. Choudhury, W. Tian, M. E. Hawley, B. Craigo, A. K. Tagantsev, X. Q. Pan, S. K. Streiffer, L. Q. Chen, S. W. Kirchoefer, J. Levy, D. G. Schlom. Room-temperature ferroelectricity in strained SrTiO₃. *Nature* **430**, 758–761 (2004).
33. E. Tsymbal. Two-dimensional ferroelectricity by design. *Science* **372**, 1389–1390 (2021).
- 10 34. R. Batra, H. D. Tran, B. Johnson, B. Zoellner, P. A. Maggard, J. L. Jones, G. A. Rossetti, R. Ramprasad. Search for Ferroelectric Binary Oxides: Chemical and Structural Space Exploration Guided by Group Theory and Computations. *Chemistry of Materials* **32**, 3823–3832 (2020).
35. R. W. Johnson, A. Hultqvist, S. F. Bent. A brief review of atomic layer deposition: from fundamentals to applications. *Materials Today* **17**, 236–246 (2014).
- 15 36. K. W. Urban, C. L. Jia, L. Houben, M. Lentzen, S. B. Mi, K. Tillmann. Negative spherical aberration ultrahigh-resolution imaging in corrected transmission electron microscopy. *Philosophical Transactions of the Royal Society A: Mathematical, Physical and Engineering Sciences* **367**, 3735–3753 (2009).
- 20 37. A. Pryor, C. Ophus, J. Miao. A streaming multi-GPU implementation of image simulation algorithms for scanning transmission electron microscopy. *Advanced Structural and Chemical Imaging* **3**,15 (2017).
38. C. Ophus. A fast image simulation algorithm for scanning transmission electron microscopy. *Advanced Structural and Chemical Imaging* **3**,13 (2017).
- 25 39. B. J. Rodriguez, C. Callahan, S. V. Kalinin, R. Proksch. Dual-frequency resonancetracking atomic force microscopy. *Nanotechnology* **18**, 475504 (2007).
40. S. Jesse, H. N. Lee, S. V. Kalinin. Quantitative mapping of switching behavior in piezoresponse force microscopy. *Review of Scientific Instruments* **77**, 073702 (2006).
- 30 41. S. Hong, J. Woo, H. Shin, J. Jeon, E. Y. Pak, E. L. Colla, N. Setter, E. Kim, K. No. Principle of ferroelectric domain imaging using atomic force microscope. *J. Appl. Phys.* **89**, 1377–1386 (2001).
42. R. K. Vasudevan, N. Balke, P. Maksymovych, S. Jesse, S. V. Kalinin. Ferroelectric or non-ferroelectric: Why so many materials exhibit “ferroelectricity” on the nanoscale. *Appl. Phys. Rev.* **4**, 021302 (2017).
- 35 43. M. Björck, G. Andersson. GenX : an extensible X-ray reflectivity refinement program utilizing differential evolution. *Journal of Applied Crystallography* **40**, 1174–1178 (2007).

44. J. Ilavsky. Nika: software for two-dimensional data reduction. *Journal of Applied Crystallography* **45**, 324–328 (2012).
45. H. A. Hsain, Y. Lee, G. Parsons, J. L. Jones. Compositional dependence of crystallization temperatures and phase evolution in hafnia-zirconia ($\text{Hf}_x\text{Zr}_{1-x}\text{O}_2$) thin films. *Applied Physics Letters* **116**, 192901 (2020).
46. A. T. Young, E. Arenholz, S. Marks, R. Schlueter, C. Steier, H. Padmore, A. Hitchcock, D. Castner. Variable linear polarization from an x-ray undulator. *J. Synch. Rad.* **9**, 270–274 (2002).
47. K. Yang, C. Hu. MOS capacitance measurements for high-leakage thin dielectrics. *IEEE Transactions on Electron Devices* **46**, 1500–1501 (1999).
48. E. D. Grimley, J. M. LeBeau. Transmission Electron Microscopy (STEM and TEM). In *Ferroelectricity in Doped Hafnium Oxide: Materials, Properties and Devices*, 317–340. Elsevier (2019).
49. X. Sang, E. D. Grimley, T. Schenk, U. Schroeder, J. M. LeBeau. On the structural origins of ferroelectricity in HfO_2 thin films. *Applied Physics Letters* **106**, 162905 (2015).
50. P. Nukala, J. Antoja-Lleonart, Y. Wei, L. Yedra, B. Dkhil, B. Noheda. Direct Epitaxial Growth of Polar $(1-x)\text{HfO}_2-(x)\text{ZrO}_2$ Ultrathin Films on Silicon. *ACS Applied Electronic Materials* **1**, 2585–2593 (2019).
51. J. M. LeBeau, A. J. D'Alfonso, N. J. Wright, L. J. Allen, S. Stemmer. Determining ferroelectric polarity at the nanoscale. *Applied Physics Letters* **98**, 052904 (2011).
52. P. Nukala, M. Ahmadi, J. Antoja-Lleonart, S. de Graaf, Y. Wei, H. W. Zandbergen, B. J. Kooi, B. Noheda. In situ heating studies on temperature-induced phase transitions in epitaxial $\text{Hf}_{0.5}\text{Zr}_{0.5}\text{O}_2/\text{La}_{0.67}\text{Sr}_{0.33}\text{MnO}_3$ heterostructures. *Applied Physics Letters* **118**, 062901 (2021).
53. Q. Luo, Y. Cheng, J. Yang, R. Cao, H. Ma, Y. Yang, R. Huang, W. Wei, Y. Zheng, T. Gong, J. Yu, X. Xu, P. Yuan, X. Li, L. Tai, H. Yu, D. Shang, Q. Liu, B. Yu, Q. Ren, H. Lv, M. Liu. A highly CMOS compatible hafnia-based ferroelectric diode. *Nature Communications* **11**, 1391 (2020).
54. C. L. Jia, M. Lentzen, K. Urban. Atomic-Resolution Imaging of Oxygen in Perovskite Ceramics. *Science* **299**, 870–873 (2003).
55. C. Jia, L. Houben, A. Thust, J. Barthel. On the benefit of the negative-spherical-aberration imaging technique for quantitative HRTEM. *Ultramicroscopy* **110**, 500–505 (2010).
56. M. H. Park, Y. H. Lee, H. J. Kim, Y. J. Kim, T. Moon, K. D. Kim, J. Müller, A. Kersch, U. Schroeder, T. Mikolajick, C. S. Hwang. Ferroelectricity and Antiferroelectricity of Doped Thin HfO_2 -Based Films. *Advanced Materials* **27**, 1811–1831 (2015).

57. F. Mehmood, T. Mikolajick, U. Schroeder. Lanthanum doping induced structural changes and their implications on ferroelectric properties of $\text{Hf}_{1-x}\text{Zr}_x\text{O}_2$ thin film. *Applied Physics Letters* **117**, 092902 (2020).
58. N. Tasneem, Y. M. Yousry, M. Tian, M. Dopita, S. E. Reyes-Lillo, J. Kacher, N. Bassiri-Gharb, A. I. Khan. A Janovec-Kay-Dunn-Like Behavior at Thickness Scaling in Ultra-Thin Antiferroelectric ZrO_2 Films. *Advanced Electronic Materials* 2100485 (2021).
59. M. H. Park, T. Schenk, C. Fancher, E. Grimley, C. Zhou, C. Richter, L. JM, J. Jones, T. Mikolajick, U. Schroeder. A comprehensive study on the structural evolution of HfO_2 thin films doped with various dopants. *J. Mater. Chem. C* **5**, 4677–4690 (2017).
60. C. Lichtensteiger, M. Dawber, and J.-M. Triscone. Ferroelectric Size Effects. In K. M. Rabe, C. H. Ahn, J.-M. Triscone, editors, *Physics of Ferroelectrics: A Modern Perspective* **105**, 305–338. Springer Berlin Heidelberg (2007).
61. P. D. Lomenzo, M. Materano, T. Mittmann, P. Buragohain, A. Gruverman, T. Kiguchi, T. Mikolajick, U. Schroeder. Harnessing Phase Transitions in Antiferroelectric ZrO_2 Using the Size Effect. *Advanced Electronic Materials* 202100556 (2021).
62. D. M. Smilgies. Scherrer grain-size analysis adapted to grazing-incidence scattering with area detectors. *Journal of Applied Crystallography* **42**, 1030–1034 (2009).
63. D.-Y. Cho, H.-S. Jung, C. S. Hwang. Structural properties and electronic structure of HfO_2 - ZrO_2 composite films. *Phys. Rev. B* **82**, 094104 (2010).
64. A. Jain, S. P. Ong, G. Hautier, W. Chen, W. D. Richards, S. Dacek, S. Cholia, D. Gunter, D. Skinner, G. Ceder, K. A. Persson. The materials project: A materials genome approach to accelerating materials innovation. *APL Materials* **1**, 011002 (2013).
65. K. Mathew, C. Zheng, D. Winston, C. Chen, A. Dozier, J. J. Rehr, S. P. Ong, K. A. Persson. High-throughput computational X-ray absorption spectroscopy. *Sci. Data* **5**, 180151 (2018).
66. R. E. Cohen. Origin of ferroelectricity in perovskite oxides. *Nature* **358**, 136–138 (1992).
67. J. Fontcuberta, D. Pesquera, G. Herranz, A. Barla, E. Pellegrin, F. Bondino, E. Magnano, F. Sa. Surface symmetry-breaking and strain effects on orbital occupancy in transition metal perovskite epitaxial films. *Nat. Commun.* **3**, 1189 (2012).
68. J. F. Ihlefeld, T. S. Luk, S. W. Smith, S. S. Fields, S. T. Jaszewski, D. M. Hirt, W. T. Riffe, S. Bender, C. Constantin, M. V. Ayyasamy, P. V. Balachandran, P. Lu, M. David Henry, P. S. Davids. Compositional dependence of linear and nonlinear optical response in crystalline hafnium zirconium oxide thin films. *Journal of Applied Physics* **128**, 034101 (2020).

69. J. Scott, J. Gardner. Ferroelectrics, multiferroics and artifacts: Lozenge-shaped hysteresis and things that go bump in the night. *Materials Today* **21**, 553–562 (2018).
70. D. D. Fong, G. B. Stephenson, S. K. Streiffer, J. A. Eastman, O. Auciello, P. H. Fuoss, C. Thompson. Ferroelectricity in Ultrathin Perovskite Films. *Science* **304**, 1650–1653 (2004).
- 5 71. D. A. Tenne, A. Bruchhausen, N. D. Lanzillotti-Kimura, A. Fainstein, R. S. Katiyar, A. Cantarero, A. Soukiassian, V. Vaithyanathan, J. H. Haeni, W. Tian, D. G. Schlom, K. J. Choi, D. M. Kim, C. B. Eom, H. P. Sun, X. Q. Pan, Y. L. Li, L. Q. Chen, Q. X. Jia, S. M. Nakhmanson, K. M. Rabe, X. X. Xi. Probing Nanoscale Ferroelectricity by Ultraviolet Raman Spectroscopy. *Science* **313**, 1614–1616 (2006).
- 10 72. A. Gruverman, M. Alexe, D. Meier. Piezoresponse force microscopy and nanoferroic phenomena. *Nature Communications* **10**, 1661 (2019).
73. N. G. Orji, M. Badaroglu, B. M. Barnes, C. Beitia, B. D. Bunday, U. Celano, R. J. Kline, M. Neisser, Y. Obeng, A. E. Vladar. Metrology for the next generation of semiconductor devices. *Nature Electronics* **1**, 532–547 (2018).
- 15 74. F. Hui, M. Lanza. Scanning probe microscopy for advanced nanoelectronics. *Nature Electronics* **2**, 221–229 (2019).
75. W. Chung, M. Si, P. R. Shrestha, J. P. Campbell, K. P. Cheung, P. D. Ye. First Direct Experimental Studies of $\text{Hf}_{0.5}\text{Zr}_{0.5}\text{O}_2$ Ferroelectric Polarization Switching Down to 100 picosecond in Sub-60mV/dec Germanium Ferroelectric Nanowire FETs. In *2018 IEEE Symposium on VLSI Technology*, 89–90 (IEEE, 2018).
- 20 76. X. Lyu, M. Si, X. Sun, M. A. Capano, H. Wang, P. D. Ye. Ferroelectric and Anti-Ferroelectric Hafnium Zirconium Oxide: Scaling Limit, Switching Speed and Record High Polarization Density. In *2019 Symposium on VLSI Technology*, T44–T45 (IEEE, 2019).
77. X. Lyu, M. Si, P. R. Shrestha, K. P. Cheung, P. D. Ye. First Direct Measurement of Sub-Nanosecond Polarization Switching in Ferroelectric Hafnium Zirconium Oxide. In *2019 IEEE International Electron Devices Meeting (IEDM)*, 15.2.1–15.2.4 (IEEE, 2019).
- 25 78. M. Si, X. Lyu, P. R. Shrestha, X. Sun, H. Wang, K. P. Cheung, P. D. Ye. Ultrafast measurements of polarization switching dynamics on ferroelectric and anti-ferroelectric hafnium zirconium oxide. *Applied Physics Letters* **115**, 072107 (2019).
- 30 79. X. Lyu, M. Si, P. R. Shrestha, J. P. Campbell, K. P. Cheung, P. D. Ye. Record Fast Polarization Switching Observed in Ferroelectric Hafnium Oxide Crossbar Arrays. In *2020 IEEE Silicon Nanoelectronics Workshop (SNW)*, 7–8 (IEEE, 2020).
80. H. Wang, Z. R. Liu, H. Y. Yoong, T. R. Paudel, J. X. Xiao, R. Guo, W. N. Lin, P. Yang, J. Wang, G. M. Chow, T. Venkatesan, E. Y. Tsybal, H. Tian, J. S. Chen. Direct observation of room-temperature out-of-plane ferroelectricity and tunneling electroresistance at the two-dimensional limit. *Nature Communications* **9**, 3319 (2018).
- 35

81. V. Garcia, S. Fusil, K. Bouzehouane, S. Enouz-Vedrenne, N. D. Mathur, A. Barthélémy, M. Bibes. Giant tunnel electroresistance for non-destructive readout of ferroelectric states. *Nature* **460**, 81–84 (2009).
82. S. Yuan, X. Luo, H. L. Chan, C. Xiao, Y. Dai, M. Xie, J. Hao. Room-temperature ferroelectricity in MoTe₂ down to the atomic monolayer limit. *Nature Communications* **10**, 1775 (2019).
83. Q. H. Qin, L. Äkäslompolo, N. Tuomisto, L. Yao, S. Majumdar, J. Vijayakumar, A. Casiraghi, S. Inkinen, B. Chen, A. Zugarramurdi, M. Puska, S. van Dijken. Resistive Switching in All-Oxide Ferroelectric Tunnel Junctions with Ionic Interfaces. *Advanced Materials* **28**, 6852–6859 (2016).
84. H. Kohlstedt, A. Petraru, K. Szot, A. Rüdiger, P. Meuffels, H. Haselier, R. Waser, V. Nagarajan. Method to distinguish ferroelectric from nonferroelectric origin in case of resistive switching in ferroelectric capacitors. *Applied Physics Letters* **92**, 062907 (2008).
85. W. Lü, C. Li, L. Zheng, J. Xiao, W. Lin, Q. Li, X. R. Wang, Z. Huang, S. Zeng, K. Han, W. Zhou, K. Zeng, J. Chen, Ariando, W. Cao, T. Venkatesan. Multi-Nonvolatile State Resistive Switching Arising from Ferroelectricity and Oxygen Vacancy Migration. *Advanced Materials* **29**, 1606165 (2017).
86. M. Qian, I. Fina, M. C. Sulzbach, F. Sánchez, J. Fontcuberta. Synergetic Electronic and Ionic Contributions to Electroresistance in Ferroelectric Capacitors. *Advanced Electronic Materials* **5**, 1800646 (2019).
87. Z. Wen, D. Wu. Ferroelectric Tunnel Junctions: Modulations on the Potential Barrier. *Advanced Materials* **32**, 1904123 (2020).
88. V. Garcia, M. Bibes. Ferroelectric tunnel junctions for information storage and processing. *Nature Communications* **5**, 4289 (2014).
89. M. C. Sulzbach, S. Estandía, X. Long, J. Lyu, N. Dix, J. Gàzquez, M. F. Chisholm, F. Sánchez, I. Fina, J. Fontcuberta. Unraveling Ferroelectric Polarization and Ionic Contributions to Electroresistance in Epitaxial Hf_{0.5}Zr_{0.5}O₂ Tunnel Junctions. *Advanced Electronic Materials* **6**, 1900852 (2020).
90. M. C. Sulzbach, S. Estandía, J. Gàzquez, F. Sánchez, I. Fina, J. Fontcuberta. Blocking of Conducting Channels Widens Window for Ferroelectric Resistive Switching in Interface-Engineered Hf_{0.5}Zr_{0.5}O₂ Tunnel Devices. *Advanced Functional Materials* **30**, 2002638 (2020).
91. B. Max, M. Pešić, S. Slesazeck, T. Mikolajick. Interplay between ferroelectric and resistive switching in doped crystalline HfO₂. *Journal of Applied Physics* **123**, 134102 (2018).

92. V. Mikheev, A. Chouprik, Y. Lebedinskii, S. Zarubin, A. M. Markeev, A. V. Zenkevich, D. Negrov. Memristor with a ferroelectric HfO₂ layer: in which case it is a ferroelectric tunnel junction. *Nanotechnology* **31**, 215205 (2020).
- 5 93. M. Materano, P. D. Lomenzo, A. Kersch, M. H. Park, T. Mikolajick, U. Schroeder. Interplay between oxygen defects and dopants: effect on structure and performance of HfO₂-based ferroelectrics. *Inorganic Chemistry Frontiers* **8**, 2650-2672 (2021).
94. R. Waser, R. Dittmann, G. Staikov, K. Szot. Redox-Based Resistive Switching Memories - Nanoionic Mechanisms, Prospects, and Challenges. *Advanced Materials* **21**, 2632–2663 (2009).
- 10 95. D. S. Jeong, R. Thomas, R. Katiyar, J. Scott, H. Kohlstedt, A. Petraru, C. S. Hwang. Emerging memories: resistive switching mechanisms and current status. *Reports on Progress in Physics* **75**, 076502 (2012).
96. H.-S. P. Wong, H.-Y. Lee, S. Yu, Y.-S. Chen, Y. Wu, P.-S. Chen, B. Lee, F. T. Chen, M.-J. Tsai. Metal–Oxide RRAM. *Proceedings of the IEEE* **100**, 1951–1970 (2012).
- 15 97. A. Chanthbouala, A. Crassous, V. Garcia, K. Bouzehouane, S. Fusil, X. Moya, J. Allibe, B. Dlubak, J. Grollier, S. Xavier, C. Deranlot, A. Moshar, R. Proksch, N. D. Mathur, M. Bibes, A. Barthélémy. Solid-state memories based on ferroelectric tunnel junctions. *Nature Nanotechnology* **7**, 101–104 (2012).
- 20 98. M. H. Park, T. Schenk, S. Starschich, C. M. Fancher, H. J. Kim, U. Böttger, C. S. Hwang, A. Toriumi, X. Tian, U. Schroeder. Effect of Surface/Interface Energy and Stress on the Ferroelectric Properties. In *Ferroelectricity in Doped Hafnium Oxide: Materials, Properties and Devices*, 145–172. Elsevier (2019).
99. M. H. Park, Y. H. Lee, T. Mikolajick, U. Schroeder, C. S. Hwang. Thermodynamic and Kinetic Origins of Ferroelectricity in Fluorite Structure Oxides. *Advanced Electronic Materials* **5**, 1800522 (2019).
- 25 100. C. Künneth, R. Batra, G. A. Rossetti, R. Ramprasad, A. Kersch. Thermodynamics of Phase Stability and Ferroelectricity from First Principles. In *Ferroelectricity in Doped Hafnium Oxide: Materials, Properties and Devices*, 245–289. Elsevier (2019).
- 30 101. H. J. Kim, Y. An, Y. C. Jung, J. Mohan, J. G. Yoo, Y. I. Kim, H. Hernandez-Arriaga, H. S. Kim, J. Kim, S. J. Kim. Low-Thermal Budget Fluorite-Structure Ferroelectrics for Future Electronic Device Applications. *physica status solidi (RRL) – Rapid Research Letters* **15**, 2100028 (2021).
- 35 102. T. Mikolajick, U. Schroeder. Ferroelectricity in bulk hafnia. *Nature Materials* **20**, 718–719 (2021).
103. C. Kittel. Theory of Antiferroelectric Crystals. *Physical Review* **82**, 729–732 (1951).

104. M. H. Park, C. S. Hwang. Fluorite-structure antiferroelectrics. *Reports on Progress in Physics* **82**, 124502 (2019).
105. K. M. Rabe. Antiferroelectricity in Oxides: A Reexamination. In *Functional Metal Oxides* 221–244. Wiley-VCH Verlag GmbH & Co (2013).
- 5 106. T. Shimizu, Y. Tashiro, T. Mimura, T. Kiguchi, T. Shiraishi, T. J. Konno, O. Sakata, H. Funakubo. Electric-Field-Induced Ferroelectricity in 5%Y-doped $\text{Hf}_{0.5}\text{Zr}_{0.5}\text{O}_2$: Transformation from the Paraelectric Tetragonal Phase to the Ferroelectric Orthorhombic Phase. *physica status solidi (RRL) – Rapid Research Letters* **15**, 2000589 (2021).
- 10 107. Y. Zheng, C. Zhong, Y. Zheng, Z. Gao, Y. Cheng, Q. Zhong, C. Liu, Y. Wang, R. Qi, R. Huang, H. Lyu. In-situ atomic visualization of structural transformation in $\text{Hf}_{0.5}\text{Zr}_{0.5}\text{O}_2$ ferroelectric thin film: from nonpolar tetragonal phase to polar orthorhombic phase. In *2021 IEEE Symposium on VLSI Technology* T16–3 (IEEE, 2021).
- 15 108. S. Lombardo, C. Nelson, K. Chae, S. Reyes-Lillo, M. Tian, N. Tasneem, Z. Wang, M. Hoffmann, D. Triyoso, S. Consiglio, K. Tapily, R. Clark, G. Leusink, K. Cho, A. Kummel, J. Kacher, A. I. Khan. Atomic-scale imaging of polarization switching in an (anti)ferroelectric memory material: Zirconia (ZrO_2). In *2020 IEEE Symposium on VLSI Technology* 1–2 (IEEE, 2020).
- 20 109. S. D. Hyun, H. W. Park, M. H. Park, Y. H. Lee, Y. B. Lee, B. Y. Kim, H. H. Kim, B. S. Kim, C. S. Hwang. Field-Induced Ferroelectric $\text{Hf}_{1-x}\text{Zr}_x\text{O}_2$ Thin Films for High- κ Dynamic Random Access Memory. *Advanced Electronic Materials* **6**, 2000631 (2020).
110. T. S. Böske, S. Teichert, D. Bräuhäus, J. Müller, U. Schröder, U. Böttger, T. Mikolajick. Phase transitions in ferroelectric silicon doped hafnium oxide. *Applied Physics Letters* **99**, 112904 (2011).
- 25 111. S. Mueller, J. Mueller, A. Singh, S. Riedel, J. Sundqvist, U. Schroeder, T. Mikolajick. Incipient Ferroelectricity in Al-Doped HfO_2 Thin Films. *Advanced Functional Materials* **22**, 2412–2417 (2012).
112. M. H. Park, C. Chung, T. Schenk, C. Richter, M. Hoffmann, S. Wirth, J. L. Jones, T. Mikolajick, U. Schroeder. Origin of Temperature-Dependent Ferroelectricity in Si-Doped HfO_2 . *Advanced Electronic Materials* **4**, 1700489 (2018).
- 30 113. P. D. Lomenzo, S. Slesazeck, T. Mikolajick, and U. Schroeder. Thickness Scaling of AFERAM ZrO_2 Capacitors with High Cycling Endurance and Low Process Temperature. In *2020 IEEE International Memory Workshop (IMW)* 1–4 (IEEE, 2020).
- 35 114. X. Luo, K. Toprasertpong, M. Takenaka, S. Takagi. Antiferroelectric properties of ZrO_2 ultra-thin films prepared by atomic layer deposition. *Applied Physics Letters* **118**, 232904 (2021).

115. R. Batra, T. D. Huan, J. L. Jones, G. Rossetti, R. Ramprasad. Factors Favoring Ferroelectricity in Hafnia: A First-Principles Computational Study. *The Journal of Physical Chemistry C* **121**, 4139–4145 (2017).
116. B. J. Kooi, B. Noheda. Ferroelectric chalcogenides—materials at the edge. *Science* **353**, 221–222 (2016).
117. D. G. Schlom, L.-Q. Chen, C. J. Fennie, V. Gopalan, D. A. Muller, X. Pan, R. Ramesh, R. Uecker. Elastic strain engineering of ferroic oxides. *MRS Bulletin* **39**, 118–130 (2014).
118. K. Yasuda, X. Wang, K. Watanabe, T. Taniguchi, P. Jarillo-Herrero. Stacking-engineered ferroelectricity in bilayer boron nitride. *Science* **372**, 1458–1462 (2021).
119. M. Vizner Stern, Y. Waschitz, W. Cao, I. Nevo, K. Watanabe, T. Taniguchi, E. Sela, M. Urbakh, O. Hod, M. Ben Shalom. Interfacial ferroelectricity by van der Waals sliding. *Science* **372**, 1462–1466 (2021).
120. Z. Zheng, Q. Ma, Z. Bi, S. de la Barrera, M.-H. Liu, N. Mao, Y. Zhang, N. Kiper, K. Watanabe, T. Taniguchi, J. Kong, W. A. Tisdale, R. Ashoori, N. Gedik, L. Fu, S.-Y. Xu, P. Jarillo-Herrero. Unconventional ferroelectricity in moiré heterostructures. *Nature* **588**, 71–76 (2020).
121. K. Chang, J. Liu, H. Lin, N. Wang, K. Zhao, A. Zhang, F. Jin, Y. Zhong, X. Hu, W. Duan, Q. Zhang, L. Fu, Q.-K. Xue, X. Chen, S.-H. Ji. Discovery of robust in-plane ferroelectricity in atomic-thick SnTe. *Science* **353**, 274–278 (2016).
122. N. Higashitarumizu, H. Kawamoto, C.-J. Lee, B.-H. Lin, F.-H. Chu, I. Yonemori, T. Nishimura, K. Wakabayashi, W.-H. Chang, K. Nagashio. Purely in-plane ferroelectricity in monolayer SnS at room temperature. *Nature Communications* **11**, 2428 (2020).
123. Z. Fei, W. Zhao, T. A. Palomaki, B. Sun, M. K. Miller, Z. Zhao, J. Yan, X. Xu, D. H. Cobden. Ferroelectric switching of a two-dimensional metal. *Nature* **560**, 336–339 (2018).
124. F. Xue, W. Hu, K. Lee, L. Lu, J. Zhang, H. Tang, A. Han, W. Hsu, S. Tu, W. Chang, C. Lien, J. He, Z. Zhang, L. Li, X. Zhang. Room-Temperature Ferroelectricity in Hexagonally Layered α -In₂Se₃ Nanoflakes down to the Monolayer Limit. *Advanced Functional Materials* **28**, 1803738 (2018).
125. L. You, F. Liu, H. Li, Y. Hu, S. Zhou, L. Chang, Y. Zhou, Q. Fu, G. Yuan, S. Dong, H. J. Fan, A. Gruverman, Z. Liu, J. Wang. In-Plane Ferroelectricity in Thin Flakes of Van der Waals Hybrid Perovskite. *Advanced Materials* **30**, 1803249 (2018).
126. F. Liu, L. You, K. L. Seyler, X. Li, P. Yu, J. Lin, X. Wang, J. Zhou, H. Wang, H. He, S. T. Pantelides, W. Zhou, P. Sharma, X. Xu, P. M. Ajayan, J. Wang, Z. Liu. Room-temperature ferroelectricity in CuInP₂S₆ ultrathin flakes. *Nature Communications* **7**, 12357 (2016).

127. A. V. Bune, V. M. Fridkin, S. Ducharme, L. M. Blinov, S. P. Palto, A. V. Sorokin, S. G. Yudin, A. Zlatkin. Two-dimensional ferroelectric films. *Nature* **391**, 874–877 (1998).
128. D. Ji, S. Cai, T. R. Paudel, H. Sun, C. Zhang, L. Han, Y. Wei, Y. Zang, M. Gu, Y. Zhang, W. Gao, H. Huyan, W. Guo, D. Wu, Z. Gu, E. Y. Tsymbal, P. Wang, Y. Nie, X. Pan. Freestanding crystalline oxide perovskites down to the monolayer limit. *Nature* **570**, 87–90 (2019).
129. P. Gao, Z. Zhang, M. Li, R. Ishikawa, B. Feng, H.-J. Liu, Y.-L. Huang, N. Shibata, X. Ma, S. Chen, J. Zhang, K. Liu, E.-G. Wang, D. Yu, L. Liao, Y.-H. Chu, Y. Ikuhara. Possible absence of critical thickness and size effect in ultrathin perovskite ferroelectric films. *Nature Communications* **8**, 15549 (2017).
130. A. Chernikova, M. Kozodaev, A. Markeev, D. Negrov, M. Spiridonov, S. Zarubin, O. Bak, Buragohain, H. Lu, E. Suvorova, A. Gruverman, A. Zenkevich. Ultrathin $\text{Hf}_{0.5}\text{Zr}_{0.5}\text{O}_2$ Ferroelectric Films on Si. *ACS Applied Materials & Interfaces* **8**, 7232–7237 (2016).
131. H. Lee, D.-h. Choe, S. Jo, J.-H. Kim, H. H. Lee, H.-j. Shin, Y. Park, S. Kang, Y. Cho, S. Park, T. Moon, D. Eom, M. Leem, Y. Kim, J. Heo, E. Lee, H. Kim. Unveiling the Origin of Robust Ferroelectricity in Sub-2 nm Hafnium Zirconium Oxide Films. *ACS Applied Materials & Interfaces* **13**, 36499–36506 (2021).
132. Z. Gao, Y. Luo, S. Lyu, Y. Cheng, Y. Zheng, Q. Zhong, W. Zhang, H. Lyu. Identification of Ferroelectricity in a Capacitor with ultra-thin (1.5-nm) $\text{Hf}_{0.5}\text{Zr}_{0.5}\text{O}_2$ Film. *IEEE Electron Device Letters* **42**, 1303–1306 (2021).

Acknowledgments: SSC and NS would like to thank Christopher Tassone, Apurva Mehta, and Kevin Stone for experimental support at SSRL, and Ramamoorthy Ramesh for access to scanning probe microscopy.

Funding: This research was supported in part by the following: the Berkeley Center for Negative Capacitance Transistors (BCNCT); Applications and Systems-Driven Center for Energy-Efficient Integrated NanoTechnologies (ASCENT), one of the six centers in the Joint University Microelectronics Program (JUMP) initiative, a Semiconductor Research Corporation (SRC) program sponsored by Defense Advanced Research Projects Agency (DARPA); the DARPA Foundations Required for Novel Compute (FRANC) program; the Interaction of Ionizing Radiation with Matter (IIRM) University Research Alliance supported by the Department of Defense (DoD); and the US Department of Energy, Office of Science, Office of Basic Energy Sciences, Materials Sciences and Engineering Division under contract no. DE-AC02-05-CH11231 (Microelectronics Co-Design program) for the development of materials for low-power microelectronics. This research used resources of the Advanced Photon Source, a U.S. Department of Energy (DOE) Office of Science user facility operated for the DOE Office of Science by Argonne National Laboratory under Contract No. DE-AC02-06CH11357. VAS and JWF were supported by the US Department of Energy, Office of Science, Basic Energy Sciences, under Award Number DE-SC-0012375. Use of the Stanford Synchrotron Radiation Light source (SSRL), SLAC National

Accelerator Laboratory, is supported by the U.S. Department of Energy, Office of Science, Office of Basic Energy Sciences under Contract No. DE-AC0276SF00515. This research used resources of the Advanced Light Source, which is a DOE Office of Science User Facility under contract no. DE-AC02-05CH11231. Electron microscopy of was performed at the Molecular Foundry, LBNL, supported by the Office of Science, Office of Basic Energy Sciences, US Department of Energy (DE-AC02-05CH11231).

Author contributions: SSC conceived the project and designed the research and experiments. SSC performed film synthesis and ferroic phase optimization. NS performed device fabrication. NS and SSC performed dielectric and electrical measurements. NS performed scanning probe microscopy. SLH performed transmission electron microscopy and analysis. YR performed second harmonic generation. SSC, CHH, VAS and JWF performed synchrotron spectroscopy (ALS, APS). SSC, NS, VAS and ZZ performed synchrotron diffraction (SSRL, APS). SSC wrote the manuscript. SSC, NS, and SS edited the manuscript. SS supervised the research.

Competing interests: Authors declare that they have no competing interests.

Data and materials availability: All data are available in the manuscript or the supplementary materials.

Supplementary Materials

Materials and Methods

Supplementary Text

Table S1

Figs. S1 to S15

References (35–132)

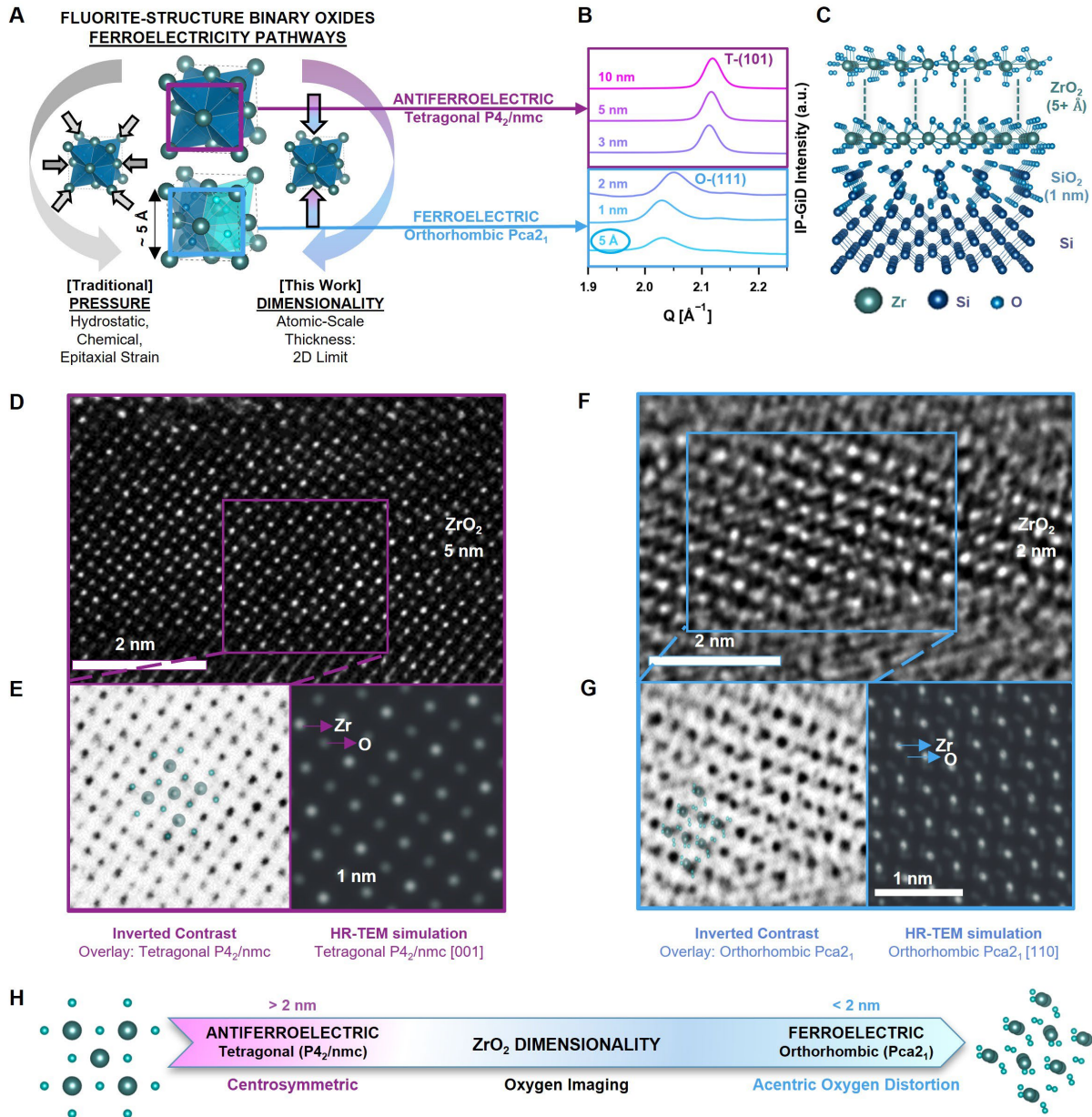


Fig. 1. Atomic-scale emergence of ferroelectricity in ZrO₂. (A) Pressure-driven pathways to ferroelectricity in fluorite-structure binary oxides; dimensionality, i.e. atomic-scale thickness scaling, can induce ferroelectric o-ZrO₂ stabilization in conventionally antiferroelectric t-ZrO₂. (B) Thickness-dependent IP-GiD demonstrating the tetragonal-to-orthorhombic phase transition in the ultrathin (5 Å-2 nm) regime (fig. S4). (C) Schematic of the Si/SiO₂(1 nm)/ZrO₂(0.5-10 nm) films grown via ALD. (D,E,F,G) Cross-sectional HR-TEM images of 5 nm ZrO₂ (D) and 2 nm ZrO₂ (F) indexed via NCSI oxygen imaging and inverted contrast HR-TEM simulations (fig. S5, S6), fit to the t-phase (E) and o-phase (G) lattice along the [001] and [110] zone axes, respectively. For inverted contrast images (E, G), light (dark) atoms represent O (Zr) atoms. Note the faint zig-zag oxygen arrangements expected for the o-phase [110] projection (G). (H) Dimensionality-driven antiferroelectric-to-ferroelectric evolution of ZrO₂ demonstrated through oxygen imaging, sensitive to the anion distortion present in fluorite-structure binary oxides.

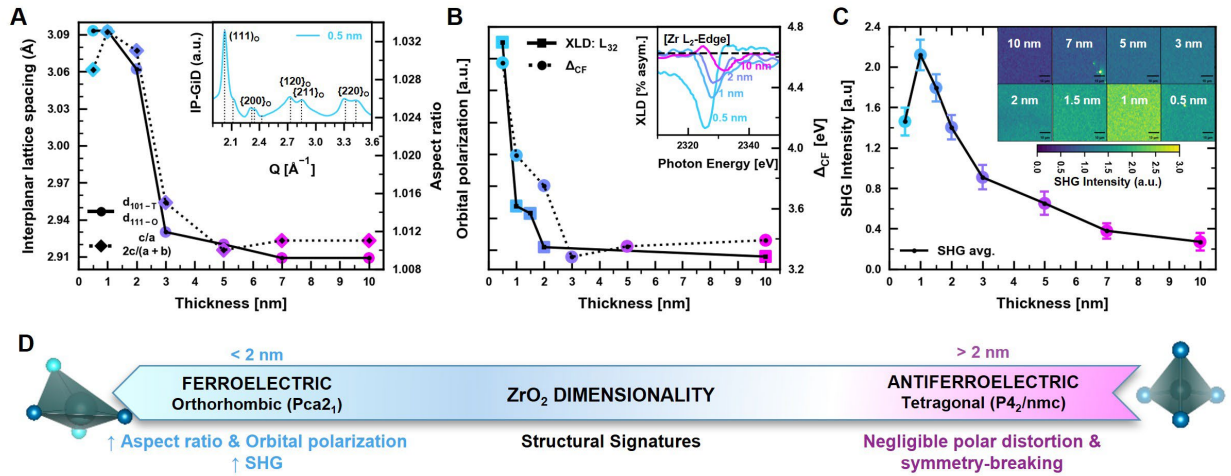


Fig. 2. Thickness-dependent ferroic phase evolution in ultrathin ZrO₂. (A) Thickness-dependent lattice spacing (t - d_{101} or o - d_{111} ; solid line; left y-axis) and aspect ratio (t -phase c/a or o -phase $2c/(a+b)$; dashed line; right y-axis) indicating ultrathin-enhanced lattice distortion. Inset: Example IP-GiD spectra for 0.5 nm ZrO₂ indexed to the ferroelectric o -phase. The structural markers for ultrathin (0.5-2 nm) and thicker (3-10 nm) ZrO₂ films are extracted from IP-GiD spectra (fig. S4) and OOP-GiD spectra, respectively (18). (B) Thickness-dependent crystal-field splitting (O K -edge XAS; solid line; left y-axis) and orbital polarization (Zr - $L_{3,2}$ -edge XLD; dashed line; right y-axis) indicating ultrathin-amplified structural and polar distortion (18) (fig. S8). Inset: Increase in orbital polarization at the Zr - L_2 -edge with decreasing ZrO₂ thickness. (C) Averaged SHG intensity of bare ZrO₂ films (0.5-10 nm) increase with decreasing ZrO₂ thickness, indicative of ultrathin-enhanced remnant polarization. Inset: 2D SHG maps for the entire ZrO₂ thicknesses series. Further evidence of strong (weak) SHG intensity in ultrathin polar (thick nonpolar) ZrO₂ samples is provided by SHG spectra (fig. S11). (D) Dimensionality-driven antiferroelectric-to-ferroelectric evolution of ZrO₂ demonstrated through various structural signatures.

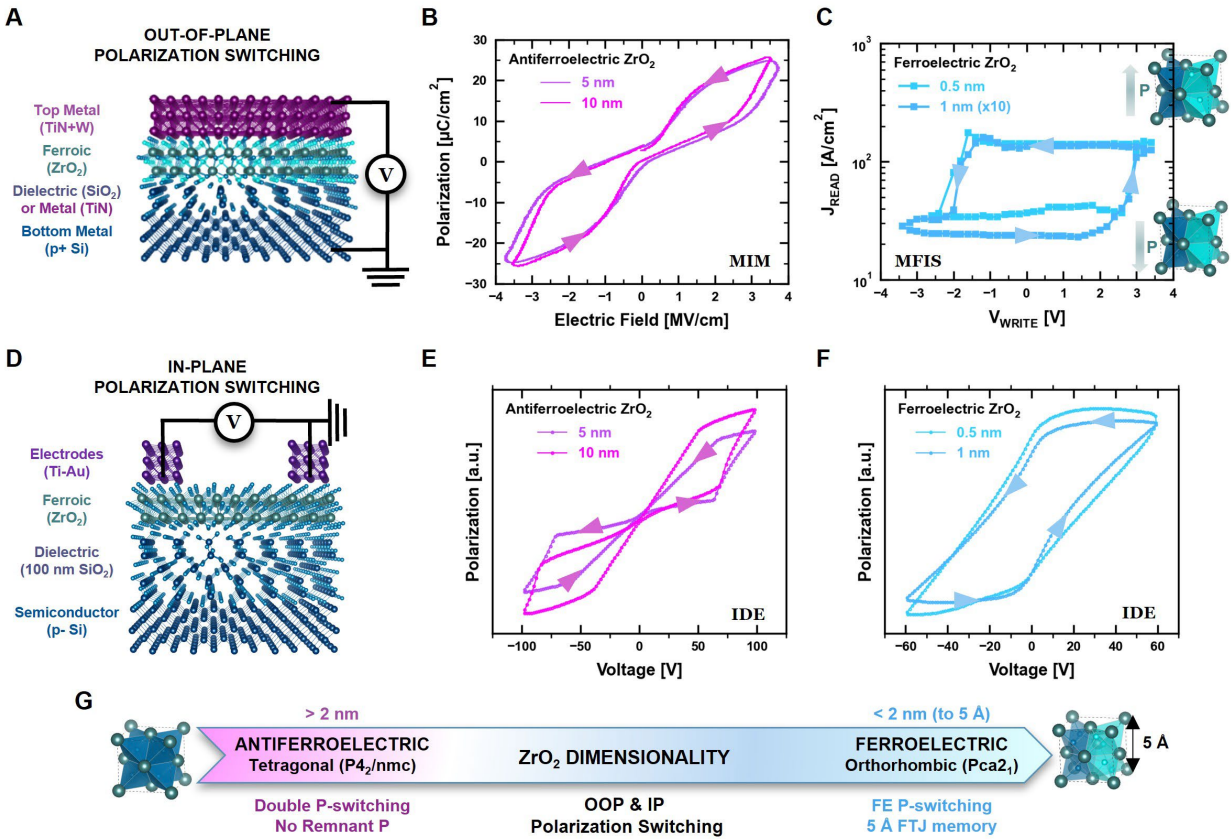


Fig. 3. Thickness-dependent polarization switching in ultrathin ZrO₂. (A) Schematic OOP capacitor geometries – MIM capacitors with bottom TiN and MFIS tunnel junctions with SiO₂ interlayer dielectrics – used to investigate thickness-dependent OOP polarization switching in ZrO₂. (B) Antiferroelectric-like OOP polarization switching observed in relatively thick (5, 10 nm) ZrO₂ from MIM P - V hysteresis loops. (C) Ferroelectric-like OOP polarization switching observed in ultrathin (5 Å, 1 nm) ZrO₂ from pulsed I - V hysteresis loops measured in MFIS tunnel junctions, demonstrating two bistable remnant resistive states, consistent with ferroelectric polarization switching and PFM hysteresis loops (fig. S14). (D) Schematic IP device geometry (IDEs) used to investigate thickness-dependent IP polarization switching in ZrO₂. (E, F) Antiferroelectric-like (E) and ferroelectric-like (F) IP polarization switching observed in relatively thick (5, 10 nm) ZrO₂ and ultrathin (5 Å, 1 nm) ZrO₂, respectively, from IDE P - V hysteresis loops. (G) Dimensionality-driven antiferroelectric-to-ferroelectric evolution of ZrO₂ demonstrated through OOP and IP polarization switching.



Supplementary Materials for

Emergent ferroelectricity in sub-nanometer binary oxide films on Si

Suraj S. Cheema, Nirmaan Shanker, Shang-Lin Hsu, Yoonsoo Rho, Cheng-Hsiang Hsu,
Vladimir A. Stoica, Zhan Zhang, John W. Freeland, Padraic Shafer, Costas P. Grigoropoulos,
Jim Ciston, Sayeef Salahuddin

Correspondence to: s.cheema@berkeley.edu, sayeef@berkeley.edu

This PDF file includes:

Materials and Methods
Supplementary Text
Table S1
Figs. S1 to S15
References 35–132

Materials and Methods

Synthesis and Processing

All thin film synthesis was performed at U.C. Berkeley; all device processing was performed at the U.C. Berkeley Marvell Nanofabrication Laboratory.

Film deposition Thin films of ZrO_2 were grown by atomic layer deposition (ALD) in a Fiji Ultratech/Cambridge Nanotech tool at 300°C in which tetrakis (ethylmethylamino) zirconium precursors are heated to 75°C and water vapor is used as the oxidant. The ALD growth technique facilitates atomic-level thickness control and conformal deposition for highly-scaled semiconductor applications (35). For metal-ferroelectric-insulator-semiconductor (MFIS) capacitor structures, 1 nm chemically-grown SiO_2 on Si was prepared by the standard clean (SC-1) solution (5:1:1 $\text{H}_2\text{O}:\text{H}_2\text{O}_2:\text{NH}_4\text{OH}$ at 80°C for 10 minutes) after the Si wafer was cleaned in Piranha (120°C for 10 minutes) to remove organics and HF (50:1 $\text{H}_2\text{O}:\text{HF}$ at room temperature for 30 s) to remove any native oxide. For interdigitated electrode (IDE) structures, 100 nm of SiO_2 is grown by thermal oxidation on Si. For metal-insulator-metal (MIM) capacitor structures, the bottom metal (TiN) is deposited by sputtering at room temperature on Si. Subsequently, ZrO_2 is deposited at 300°C by ALD in which 10 ALD cycles corresponds to one nanometer of ZrO_2 film, as confirmed by X-ray reflectivity and out-of-plane grain size analysis (fig. S1). Finally, for MFIS and MFM structures, the top metal (TiN and/or W) is deposited by sputtering at room temperature. For bare ferroelectric films (structural and optical studies), the top metal is not deposited.

Capacitor fabrication For MFIS and MFM capacitor structures (P - V , C - V and I - V characterization), micron-sized top electrodes of various areas are defined by photolithography and selective etching of the top TiN and/or W metal layer.

Interdigitated electrode fabrication For in-plane interdigitated electrode (IDE) device structures, 1-5 μm spaced IDEs are patterned by lift-off photolithography on bare ZrO_2 films grown on 100 nm of thermal SiO_2 . The metal electrodes (Ti(5 nm)/Au(120 nm)) are then deposited with e-beam evaporation.

Transmission Electron Microscopy

HR-TEM Electron microscopy was performed at the National Center for Electron Microscopy (NCEM) facility of the Molecular Foundry at Lawrence Berkeley National Laboratory (LBNL). High-resolution transmission electron microscopy (HR-TEM) images of 5 nm and 2 nm ZrO_2 were performed by aberration-corrected FEI ThemIS 60-300 STEM/TEM microscope operated at 300 kV using a TEM mode for atomic scale imaging. In order to precisely identify the fluorite-structure in ultrathin ZrO_2 films, the NCSI technique was employed to probe not only the zirconium sublattice, but also the oxygen sublattice. The cross-sectional TEM samples of 5 nm and 2 nm ZrO_2 were mechanically polished using an Allied High Tech Multiprep at a 0.5° wedge. After thinning the total thickness of samples down to 10 μm , the specimens were Ar ion milled using a Gatan Precision Ion Milling System to an electron-transparent specimen starting from 4 keV down to 200 eV as the final cleaning energy.

NCSI and HR-TEM Simulations For the NCSI technique, the oxygen atoms are expected to be visible for specimen thicknesses below ~ 10 nm (36); therefore, the experimental HR-TEM data was acquired at similarly thin specimen thicknesses. From HR-TEM imaging, the oxygen atoms became apparent under the following experimental conditions: tuning the defocus (C_1) at spherical aberration (C_s) values of $C_3 = -16 \mu\text{m}$ and $C_5 = 6.8$ mm. The HR-TEM image simulations were calculated using the Prismatic method (37,38) under the specified experimental conditions. After tuning the defocus (~ 2 to 4 nm) in tandem with the slice thickness (~ 20 Å) and specimen thickness (below 12.5 nm) (fig. S6), the oxygen atoms were clearly visible within the zirconium sublattice. In general, the grain size along the beam direction is comparable to the grain width parallel to the interface for the same image, which is ~ 5 - 15 nm (fig. S3); therefore, it is reasonable for the specimen thickness to range around the ZrO_2 grain size. Based on these experiment-guided conditions, the HR-TEM simulations for the tetragonal $P4_2/nmc$ (specimen thickness = 9.8 nm and defocus = 4 nm) and orthorhombic $Pca2_1$ (specimen thickness = 9.81 nm and defocus = 4 nm) were found to match well with the experimental data for 5 nm and 2 nm ZrO_2 films, respectively (Fig. 1E,G).

HAADF-STEM Wide field-of-view and local imaging of 5 ALD cycle (~ 0.5 nm) ZrO_2 thin films were performed by high-angle annular dark-field scanning transmission electron microscopy (HAADF-STEM) at 300 kV to confirm the wide-area stability and thickness of ultrathin ZrO_2 , respectively (fig. S2). The ultrathin ZrO_2 layer was surrounded by high contrast neighboring layers (low-Z SiO_2 underlayer and low-Z Al_2O_3 capping layer) to aid in layer delineation.

Scanning Probe Microscopy

Atomic force microscopy (AFM) and piezoresponse force microscopy (PFM) measurements were performed using a commercial scanning probe microscope (Asylum MFP-3D) at UC Berkeley. Dual-frequency resonance-tracking PFM (39) was conducted using a conductive Pt/Ir-coated probe tip (NanoSensor PPP-EFM) to measure switching-spectroscopy (SS) (40) piezoresponse hysteresis loops (fig. S14C) and image written domain structures (fig. S13). Resonance-enhanced PFM increases the signal to noise ratio for the detection of out-of-plane electric polarization, critical for ultrathin films. Contact was made to the bottom TiN electrode or heavily doped Si electrode for all PFM studies. For bare imaging studies, contact was made to the bare ZrO_2 surface. Switching spectroscopy hysteresis loops were measured on capacitor structures to help eliminate electrostatic artifacts from the tip (41), mitigate possible electromechanical contributions (42), and to yield more confined electric fields.

Optical Characterization

The second harmonic generation (SHG) measurement geometries are sensitive to in-plane inversion symmetry breaking in the ferroelectric ZrO_2 thin films (see Supplementary Text section “SHG sensitivity to in-plane polarization”).

SHG mapping Second harmonic generation (SHG) spatial mapping measurements (Fig. 2C) were performed with a Ti:sapphire femtosecond laser (Tsunami, Spectra Physics, $\lambda \sim 800$ nm, frequency ~ 80 MHz). The linearly polarized femtosecond laser beam was focused through $50\times$ objective lens ($\text{NA} \sim 0.42$) which results in a focal spot size of $2 \mu\text{m}$. The generated SHG signal was collected through the same objective lens and separated from the fundamental beam by the

harmonic separator. After passing through the optical bandpass filter, the SHG signals were registered to the photon multiplier tube (PMT) without a polarizer. The fundamental beam was mechanically chopped, and the signal collected by the PMT was filtered by a lock-in amplifier to reduce the background noise. For SHG spatial mapping, a two-axis piezo stage was utilized and the coordinate was synchronized with the PMT signal (fig. S12A). The SHG intensity was obtained by averaging the mapping signals across a $100\ \mu\text{m} \times 100\ \mu\text{m}$ sample area.

SHG spectrum For SHG emission spectrum measurement, the optical beam path was the same as the setup for SHG mapping, except for the laser wavelength, optical filter, and photon detection components (fig. S12B). SHG spectrum measurements were performed with a Ti:sapphire femtosecond laser with 810 nm of wavelength (Tsunami, Spectra Physics, $f \sim 80$ MHz, pulse duration ~ 100 fs). The generated SHG signal was collected by a spectrometer (PI Max, Princeton Instrument) without signal demodulation after filtering by a 700 nm short-pass filter to block the fundamental laser beam at 810 nm.

X-ray Characterization

Accounting for different X-ray wavelengths XRR, OOP-GiD, and IP-GiD data is plotted in terms of Q ($1/\text{\AA}$) rather than 2θ ($^\circ$) such that X-ray data measured at various synchrotron beamlines are plotted on a consistent scale, where Q is defined as

$$Q = \frac{4\pi}{\lambda} \sin \frac{2\theta}{2}$$

where 2θ refers to the detector angle at a given X-ray wavelength λ , which varies across the different synchrotron measurement setups.

X-ray reflectivity Synchrotron X-ray reflectivity (XRR) – performed at Sector 33-BM-C beamline of the Advanced Photon Source, Argonne National Laboratory and at Beamline 2-1 of the Stanford Synchrotron Radiation Lightsource, SLAC National Accelerator Laboratory – confirmed the thickness of ultrathin ZrO_2 films (fig. S1A). Fitting analysis (fig. S1B) was performed with the python package GenX (43).

Grazing incidence diffraction: out-of-plane Synchrotron out-of-plane grazing-incidence diffraction (GID) was performed at Beamline 2-1 of the Stanford Synchrotron Radiation Lightsource, SLAC National Accelerator Laboratory with grazing angles $\theta < 0.2^\circ$ (fig. S1C). The X-ray source was fixed at 17 keV ($\lambda = 0.729\ \text{\AA}$). The high flux from the synchrotron source enabled collection of sufficient diffraction intensity from the few crystallographic planes present in ultrathin ZrO_2 films.

Grazing incidence diffraction: in-plane Synchrotron in-plane grazing-incidence diffraction (GID) (Fig. 1B, fig. S4) was performed at Sector 33-ID-D beamline of the Advanced Photon Source, Argonne National Laboratory. A Pilatus-II 100K Area Detector mounted on the del-arm was used to collect diffraction signal with a grazing incidence geometry. The region-of-interest on the detector was set such that the ring-like signal was fully integrated. In-plane GID was collected by sweeping the in-plane angle ν (8 - 50°) with a fixed out-of-plane grazing angle δ ($\delta = 0.9^\circ$); the corrected Bragg angle (2θ) over which the data is plotted and indexed is determined from the relationship $\cos(2\theta) = \cos(\nu) \cdot \cos(\delta)$ set by the geometry of the diffractometer. The X-

ray source was fixed at 16 keV ($\lambda = 0.775 \text{ \AA}$). In-plane diffraction yields more diffraction peaks with better defined width, likely due to the preferred orientation and disc-shape domains in the film. Therefore, in-plane GID enables clear indexing to the ferroelectric orthorhombic ($Pca2_1$) and antiferroelectric tetragonal ($P4_2/nmc$) fluorite structure in the ultrathin HfO_2 - ZrO_2 films, as the presence of many reflections from the in-plane GID spectra (fig. S4) allow for clear distinction from other nonpolar fluorite-structure polymorphs. Such diffraction spectra would be otherwise prohibited in typical out-of-plane geometry due to the lack of vertical diffraction planes and the large linewidth inherent to ultrathin films.

Two-dimensional diffraction Two-dimensional reciprocal space maps (fig. S3C-F) were measured at Beamline 11-3 of the Stanford Synchrotron Radiation Lightsource, SLAC National Accelerator Laboratory. Rayonix MX225 CCD area detector collected diffraction flux in the grazing incidence ($\theta < 0.20^\circ$) geometry; the X-ray source (50 microns vertical x 150 microns horizontal beam size) was fixed at 12.7 keV. The sample-detector work distance was set to 80 mm to enable detection of a wide region of reciprocal space (Q -range 0.2 to 5 \AA^{-1}) at the expense of reciprocal space resolution, set by the pixel size. The two-dimensional diffraction scans – in which a wide portion of the entire reciprocal space was collected simultaneously, rather than at discrete regions in Q_x - Q_y space – were averaged over data collection time and for repeated scans. These measurement features, in tandem with the high X-ray flux afforded by the synchrotron source, enabled sufficient diffraction signal detection and contrast in films just 1 nm in thickness. Data analysis was performed Nika, an Igor Pro package for correction, calibration and reduction of two-dimensional areal maps into one-dimensional data (44). Two-dimensional reciprocal space maps on bare ZrO_2 heterostructures confirm the presence of crystalline ultrathin films despite the low deposition temperature, afforded by the low crystallization temperature of ZrO_2 on Si (45).

X-ray absorption spectroscopy and X-ray linear dichroism Hard and soft synchrotron X-ray spectroscopy (Fig. 2B, fig. S8) was measured at beamline 4-ID-D of the Advanced Photon Source, Argonne National Laboratory and Beamline 4.0.2. of the Advanced Light Source, Lawrence Berkeley National Laboratory, respectively. Spectroscopy measurements were taken at the oxygen K -edge (520-550 eV), zirconium $M_{3,2}$ -edge (325-355 eV) and zirconium $L_{3,2}$ -edge (2200-2350 eV). X-rays were incident at 20° off grazing. XAS (XLD) was obtained from the average (difference) of horizontal and vertical linearly polarized X-rays. To eliminate systematic artifacts in the signal that drift with time, spectra measured at ALS were captured with the order of polarization rotation reversed (e.g., horizontal, vertical, vertical, and horizontal) in successive scans, in which an elliptically polarizing undulator tuned the polarization and photon energy of the synchrotron X-ray source (46). Spectra measured at APS were recorded under various modes: total electron yield (TEY), fluorescence yield (FY), and reflectivity (REF).

Dielectric and electrical measurements

Metal-oxide-semiconductor (MOS) capacitance Capacitance-voltage (C - V) measurements (fig. S9) were performed using a commercial Semiconductor Device Analyzer (Agilent B1500) with a multi-frequency capacitance measuring unit (MFCMU). 19 micron W tips (d.c.P-HTR 154001, FormFactor) made electrical contact within a commercial probe station (Cascade Microtech); voltage was applied to the top electrode and the lightly-doped Si bottom electrode

was grounded. To eliminate contributions from series and parallel parasitic resistances, frequency-dependent C - V measurements were performed. In particular, C - V data was analyzed at two frequencies (100 kHz-1 MHz) to allow for the extraction of accurate frequency-independent C - V via a three-element circuit model consisting of the capacitor and the series and parallel resistors (47). The frequency-independent capacitance is given by,

$$C = \frac{f_1^2 C_1 (1 + D_1^2) - f_2^2 (1 + D_2^2)}{f_1^2 - f_2^2}$$

where C_i and D_i refer to the measured capacitance in parallel mode (C_p - R_p) and dissipation values at frequency f_i . The dissipation factor is given by $D = -\cot(\theta)$, where θ is the phase angle. In order to maximize the accuracy of this method, it is important the dissipation factors are small ($\ll 1$) at the frequencies chosen; therefore, high frequencies (100 kHz-1 MHz) were selected.

Metal-insulator-metal (MIM) polarization Polarization-voltage (P - V) measurements on MIM capacitors (Fig. 3A) were performed using a Agilent 81150A Pulse Function Arbitrary Noise Generator/InfiniiVision DSOX3024A oscilloscope setup. 19 micron W tips (d.c.P-HTR 154001, FormFactor) made electrical contact within a commercial probe station (Cascade Microtech); voltage was applied to the top electrode and the bottom TiN electrode was grounded. A bipolar triangular waveform was applied at frequencies ~ 10 kHz to obtain P - V loops for relatively thick (5, 10 nm) antiferroelectric ZrO₂ films (Fig. 3B).

Interdigitated electrode (IDE) polarization Polarization-voltage (P - V) measurements on IDE structures (Fig. 3D) were performed using a Radiant ferroelectric tester, which enables the application of high voltages (up to 100 V) required to measure micron-spaced IDE devices. A bipolar triangular waveform was applied at frequencies ~ 10 kHz to obtain P - V loops for relatively thick antiferroelectric ZrO₂ and ultrathin ferroelectric ZrO₂ films (Fig. 3E,F, fig. S10). In-plane P - V loops were measured on ZrO₂ samples deposited on thick (100 nm) SiO₂-buffered Si to minimize parasitic capacitance contributions from the underlying Si substrate.

Temperature-dependent polarization In-plane P - V loops were measured for 0.5 nm ZrO₂ IDE structures as a function of temperature (fig. S15) using a Neocera heating stage attached to a probe station equipped with a Radiant ferroelectric tester. The IDE sample was pasted to thermally-conductive, electrically-insulating AlN to eliminate charge contributions from the heating coils during P - V measurements. P - V loops were collected ranging from 25°C to 175°C in 25°C increments across 60 V bipolar hysteresis sweeps.

Metal-ferroelectric-insulator-semiconductor (MFIS) pulsed I - V measurements Pulsed tunnel current measurements were performed on MFIS capacitors (Fig. 3A) using a commercial Semiconductor Device Analyzer (Agilent B1500). Pulsed I - V_{write} hysteresis maps (Fig. 3C, fig. S14D) were constructed using an arbitrary linear waveform generator (ALWG) to apply write voltages with progressively different amplitudes, followed by a read pulse at 200 mV (fig. 14B). Voltage was applied to the top electrode and the heavily-doped Si bottom electrode was grounded (fig. 14A).

Supplementary Text

Thickness Analysis

Local and global probes At the ultrathin thickness regime, the global nature of X-ray analysis can lead to more representative thickness determination than the local nature of TEM. In particular, X-rays at the grazing angles of $\theta = 0.1-0.2^\circ$ employed for XRR and GiD studies (fig. S1) have a sample footprint over 50 mm for the 200 μm X-ray spot sizes used at the respective synchrotron beamlines. Considering the sample sizes used for synchrotron X-ray studies were ~ 25 mm long (cut from 6" wafers), the entire sample area, along the beam direction, was covered by the grazing incident X-rays. Meanwhile, TEM images only probe \sim hundreds of nanometers in its widest field-of-view (fig. S2A). Therefore, the global-nature of the grazing-angle X-ray measurements probes orders of magnitude larger sample area, enabling a more representative determination of the thickness.

Wide area uniformity ALD is renowned for its wafer-scale uniformity and angstrom-level thickness precision derived from its self-limiting reaction (35). Therefore, as expected, wide field-of-view TEM of 0.5 nm ZrO_2 (fig. S2A) illustrates the ultrathin ZrO_2 layer is continuous across a large area (~ 350 nm). Furthermore, as mentioned in the previous section, the X-ray beam footprint in the grazing incidence XRR and OOP diffraction experiments (tens of millimeters) provide additional thickness verification across a much wider area (Fig. S1) compared to the TEM imaging (hundreds of nanometers).

XRR X-ray reflectivity (XRR) fitting analysis (fig. S1B) was performed with the python package GenX (43), in which the underlying SiO_2 buffer layer and top ZrO_2 layer thicknesses were fitting parameters for ZrO_2 films ranging from 5 to 100 ALD cycles in thickness. The extracted growth rate from XRR is 0.97 \AA ZrO_2 per ALD cycle (fig. S1B), which is close to the commonly reported ~ 1 $\text{\AA}/\text{cycle}$ growth rate for ALD-grown HfO_2 - ZrO_2 (11). Furthermore, the growth rate is consistent with that extracted from out-of-plane (OOP) grain size analysis (fig. S1D).

Grain Size The out-of-plane (OOP) grain sizes (D) were determined via Scherrer's equation (62),

$$D = \frac{2\pi}{\Delta Q}$$

where $\Delta Q = \frac{4\pi \cos(\theta)\Delta(2\theta)}{2\lambda}$, θ corresponds to either the $(101)_t$ peak or the $(111)_o$ peak, and $\Delta(2\theta)$ is the full width at half maximum (FWHM). The above equation was applied to the OOP-GID spectra for the ZrO_2 thickness series (fig. S1C). For ZrO_2 films below 10 nm (≤ 7 nm), the OOP grain size is constrained by the ZrO_2 physical thickness (fig. S1D); therefore, OOP grain size in the ultrathin limit serves as a gauge of the ZrO_2 thickness. The growth rate determined from this analysis (0.93 \AA ZrO_2 per ALD cycle) is consistent with that determined from XRR (fig. S1B).

TEM The confirm the thickness of the 5 ALD cycle thick ZrO_2 layer, local cross-section HR-STEM images (fig. S2) were analyzed with DigitalMicrograph software using a line profile ~ 3 nm with integration width ~ 30 nm. Due to the angstrom-level roughness, the red boundary lines are determined by eye based on layer color contrast; the ultrathin ZrO_2 layer was surrounded by

high contrast neighboring layers (low-Z SiO₂ underlayer and low-Z Al₂O₃ capping layer) to aid in layer delineation. Slight roughness is expected due to the non-sharp interfaces present in non-epitaxial ALD-grown films on non-crystalline templates (e.g. amorphous SiO₂). Furthermore, beam damage from milling during TEM sample preparation could potentially introduce another source of roughness. On the other hand, no sample preparation is required for XRR and X-ray based measurements, just the uncapped ZrO₂ film is necessary. These contributions help explain why the thickness extracted from the local TEM imaging (fig. S2C, 0.58 nm) is slightly thicker than the thickness extracted from the grazing X-ray techniques (fig. S1, ~ 0.5 nm).

Structural Analysis

Oxygen imaging analysis Original atomic-resolution studies of HfO₂-ZrO₂-based ferroelectrics employed high-angle annular dark-field scanning transmission electron microscopy (HAADF STEM) to identify various fluorite-structural polymorphs (48). While this technique can successfully identify various fluorite-structure polymorphs in HfO₂-ZrO₂ thin films (10, 49, 50), it is not sensitive to subtle oxygen acentric displacements; HAADF STEM contrast preferentially highlights the more strongly scattering cation atoms relative to the more weakly scattering oxygen anions. Other works aimed to distinguish the different orthorhombic space groups based on mirror symmetry-breaking employed the position-averaged convergent beam electron diffraction (PACBED) method (51), which implies the existence of non-centrosymmetric orthorhombic *Pca2*₁ structure in doped-HfO₂ thin films (49); however, this technique still does not provide definitive evidence of the polar *Pca2*₁ phase.

To address this limitation, electron microscopy work shifted to oxygen-sensitive techniques to more directly identify the ferroelectric phases in this material system, which included integrated differential phase contrast (iDPC) STEM (19,52), aberration-corrected STEM-ABF (53) and negative spherical aberration imaging (NCSI) (20). In this work, we employ the NCSI technique for oxygen imaging analysis (54, 55), in which the oxygen atoms can become visible under certain experimental conditions. The HR-TEM image simulations (37, 38) were calculated close to the experimental imaging conditions (Materials and Methods, fig. S6) along various zone axes for the tetragonal *P4*₂/*nmc* structure and the orthorhombic *Pca2*₁ structure (fig. S5) to match with the experimental HR-TEM imaging of 5 nm ZrO₂ and 2 nm ZrO₂ (Fig. 1), respectively. In particular, the HR-TEM simulation of the orthorhombic *Pca2*₁ along the [110] zone axis under the experimental NCSI conditions clearly demonstrate alternating rows of zig-zag and blurred oxygen arrangements, which match well with the experimental data for 2 nm ZrO₂ films (Fig. 1G, fig. S6).

Cation imaging analysis Beyond oxygen imaging analysis, traditional cation imaging can also provide supplemental confirmation of the crystal structures indexed by NCSI. In particular, the cation-cation bond angle between neighboring Zr atoms demonstrate a very close match to HRTEM simulations (fig. S7) for both the tetragonal *P4*₂/*nmc* structure (5 nm ZrO₂ films) and the orthorhombic *Pca2*₁ structure (2 nm ZrO₂ films) along the [001] and [110] zone axes, respectively.

Ferroic phase identification via diffraction analysis For fluorite-structure thin films, the main structural polymorphs to consider are the dielectric monoclinic (*P2*₁/*c*), antiferroelectric tetragonal (*P4*₂/*nmc*), and ferroelectric orthorhombic (*Pca2*₁) phases. Various diffraction

reflections from the wide-angle GiD spectra enable indexing to the orthorhombic $Pca2_1$ and tetragonal $P4_2/nmc$ phases. Lattice parameters (a , b , c) – determined via Bragg’s law from the d_{200} family of reflections – are self-consistently checked against the (111) ($\frac{1}{d_{111}^2} = \frac{1}{a^2} + \frac{1}{b^2} + \frac{1}{c^2}$) and (101) ($\frac{1}{d_{101}^2} = \frac{1}{a^2} + \frac{1}{c^2}$) lattice spacings, as well as other higher-order reflections, for the ferroelectric o-phase and antiferroelectric t-phase, respectively (fig. S4). The presence of monoclinic phase fraction is ruled out based on the lack of its characteristic split {111} reflections in the diffraction spectra, which would have been sufficiently separated from the (111)_o and (101)_t reflections. The tetragonal (101)_t reflection is distinguished from the orthorhombic (111)_o reflection in ultrathin (2 nm and below) films (Fig. S4D-F) based on the self-consistent indexing methodology detailed above. From the indexing analysis, we find the tetragonal (101)_t reflection has a smaller d -spacing than the orthorhombic (111)_o reflection, consistent with results in thicker HfO₂-ZrO₂-based films (56,57).

Structural distortion analysis: aspect ratio The aspect ratios (Fig. 2A) of the antiferroelectric t-phase (c/a) and the ferroelectric o-phase ($2c/(a + b)$) provide an indication of the degree of lattice distortion present in their respective structures, as recently investigated for ALD-grown ferroelectric Zr:HfO₂ films (11) and ALD-grown antiferroelectric ZrO₂ films (58). The aspect ratios were computed from the extracted lattice parameters based on the self-consistent indexing methodology detailed above. In particular, the aspect ratio of the o-phase exceeds that of the t-phase for fluorite-structure oxides (56,59). Notably, the lattice distortion present in ZrO₂ is enhanced in the ultrathin regime – opposite to the typical tetragonal distortion trend in perovskite ferroelectrics (60) – indicative of the "reverse" size effects present in fluorite-structure ferroelectrics. For example, the tetragonal aspect ratio was shown to decrease with decreasing thickness in ferroelectric PbTiO₃ films (60), while the orthorhombic aspect ratio is substantially enhanced in the ultrathin regime for fluorite-structure Zr:HfO₂ films (11).

Structural distortion analysis: interplanar lattice spacing Another structural marker, the interplanar lattice spacing (d_{101-t} , d_{111-o}), also indicates ultrathin-amplified distortions in the ZrO₂ films (Fig. 2A). The origin of the left-shift in the (111)_o ((101)_t) reflection with decreasing thickness is typically attributed to the phase fraction distribution from the antiferroelectric t-phase towards the ferroelectric o-phase; the left-shift of the peak in reciprocal space corresponds to an increase in real-space lattice spacing. In particular, the ferroelectric o-phase d_{111} -spacing (>3.03 Å) for ZrO₂ in the ultrathin regime (< 2 nm) is larger than typical values for thick ferroelectric HZO films (2.95 Å) (21), demonstrating that ZrO₂ is in fact strained i.e. increased rhombic distortion. This is consistent with the ultrathin-enhanced lattice distortions trend observed in previous ALD-grown highly-oriented orthorhombic ferroelectric Zr:HfO₂ films (11) as well as PLD-grown epitaxial orthorhombic ferroelectric Zr:HfO₂ films (26). On the other hand, we observe that the t-phase d_{101} spacing (2.91-2.95 Å) in thicker ZrO₂ films (~4-10 nm) is nearly the same as is expected for prototypical antiferroelectric t-ZrO₂ (2.94 Å) (21). This is expected: when the tetragonal phase is strained with decreasing thickness, it transitions to the lower symmetry orthorhombic phase as opposed to remaining in the tetragonal phase, as it does not have the same tolerance of the FE o-phase to maintain its symmetry when strained. Consequently, the larger d -spacing is attributed to the FE o-phase (56), as confirmed by self-consistent indexing to higher-order reflections (fig. S4). These results, along with the findings reported in previous ALD-grown highly-oriented orthorhombic ferroelectric Zr:HfO₂ films (11),

ALD-grown polycrystalline antiferroelectric ZrO₂ films (58,61), as well as PLD-grown epitaxial orthorhombic ferroelectric Zr:HfO₂ films (26), indicate ultrathin-enhanced lattice distortions might be inherent to the symmetry present in fluorite-structure oxides, in stark contrast to the size effects typically present in the prototypical perovskite-structure oxide ferroelectrics (6,7).

Crystal field splitting X-ray spectroscopy provides various signatures to distinguish the competing ferroelectric o-phase and antiferroelectric t-phase in fluorite-structure thin films (11,63). Simulated XAS spectra for ZrO₂ in the various fluorite-structure polymorphs (orthorhombic *Pca2*₁ and tetragonal *P4*₂/*nmc*) were computed through the Materials Project (64) open-source database for XAS spectrum (65); previous work on ultrathin ferroelectric Zr:HfO₂ films (11) provides additional details on the symmetry-specific spectroscopic signatures. The t-phase (*P4*₂/*nmc*) nonpolar distortion (*D*_{4h}, 4-fold prismatic symmetry) from regular tetrahedral (*T*_d, full tetrahedral symmetry) fluorite-structure symmetry does not split the degenerate *e*-bands (*d*_{*x*²-*y*²}, *d*_{*3z*²-*r*²}), as confirmed by experiment (63) and the aforementioned XAS simulations. Meanwhile, the o-phase (*Pca2*₁) polar rhombic pyramidal distortion (*C*_{2v}, 2-fold pyramidal symmetry) does split the *e* manifold based on crystal field symmetry, providing a spectroscopic means to distinguish the tand o-phases i.e. the additional spectroscopic feature present between the main *e*- and *t*₂- absorption features due to this additional symmetry-lowering distortion. The O *K*-edge XAS spectra demonstrates tetrahedral and rhombic splitting features closely matching the polar o-phase (*Pca2*₁) emerging for ZrO₂ in the sub-2 nm range, indicative of the ultrathin-enhanced emergence of the ferroelectric o-phase. This demonstrates a spectroscopic fingerprint for phase identification beyond diffraction which can often be ambiguous due to the nearly identical t- and o-phase lattice parameters (56). The symmetry-specific crystal field distortions in ZrO₂ films also evolve with thickness; the tetrahedral (rhombic) crystal field Δ_T (Δ_R) arising from the *T*_d (*C*_{2v}) symmetry in ultrathin ZrO₂ films sharply increases below 3 nm thickness (Fig. 2B), suggesting the increased emergence of ferroelectric o-ZrO₂ in ultrathin films, consistent with thickness-dependent diffraction trends (Fig. 2A)

Orbital polarization In conjunction with XAS, x-ray linear dichroism (XLD) can also probe structural distortions due to its sensitivity to orbital asymmetry, which can arise from inversion symmetry breaking. For example, in perovskite ferroelectrics PbTiO₃ and BaTiO₃, the Ti 3*d* - O 2*p* orbital hybridization is essential for stabilizing the noncentrosymmetric ferroelectric structure (66). Particularly at the 3*d* cation *L*_{3,2} edge, orbital polarization extracted from XLD is used as a measure of the oxygen octahedral distortion in perovskites due to the anisotropic hybridization between cation 3*d* and O 2*p* orbitals (67). Accordingly, in fluorite-structure ferroelectrics, the magnitude of XLD present at the Zr *M*_{3,2} and Zr *L*_{3,2} edges can be a gauge of the degree of polyhedral distortion – in this case distortion of oxygen tetrahedron – and the oxygen atomic asymmetry (11). Indeed, the orbital polarization at these Zr edges is enhanced as the thickness is reduced from the thick (10 nm) to ultrathin (5 Å) regime (fig. S8D), consistent with diffraction results also demonstrating amplified structural distortions in the ultrathin limit.

Optical Analysis

Polarization insights from SHG Nonlinear optical microscopy also supports the size-dependent ferroic phase evolution, as the observed increase in second harmonic generation (SHG) signal with decreasing ZrO₂ thickness (Fig. 2C, fig. S11) is consistent with the structural

trends indicating the ultrathin-enhanced FE polarization (Fig. 2A,B). Indeed, SHG intensity has been shown to directly map to the polarization across the composition space in 20 nm thick HfO₂-ZrO₂ solid solutions (68). The exception to the ultrathin-enhanced polarization trend from SHG spatial mapping measurements (Fig. 2C) occurs for 5 Å ZrO₂, which can be potentially attributed to an amorphous phase fraction expected in such ultrathin films deposited at low temperature (300°C). The SHG spot size can engulf both crystalline regions in the polar o-phase and amorphous regions, so the averaged SHG signal can be weighed down by this amorphous fraction; meanwhile, the other structural signatures (Fig. 2A,B) are only sensitive to the crystalline regions.

SHG sensitivity to in-plane polarization In the SHG measurement configuration (fig. S12), a linearly polarized femtosecond laser beam impinges on the sample surface in the normal direction, which results in in-plane polarization electric field. According to the assigned physical coordinate with respect to the lab coordinate for in-plane polarized regions of sample, the electric field of fundamental light has components $\mathbf{E}^\omega(\theta) = (-E_0 \sin\theta, 0, E_0 \cos\theta)$. Here, θ is the azimuthal angle of the fundamental light polarization, and the ω subscript denotes the frequency of the fundamental light.

The light-induced nonlinear polarization in the in-plane polarized regions of the Pca2₁ structure ($2mm$ point group) can be obtained as follows:

$$\begin{pmatrix} P_x \\ P_y \\ P_z \end{pmatrix} = \begin{bmatrix} 0 & 0 & 0 & 0 & d_{15} & 0 \\ 0 & 0 & 0 & d_{15} & 0 & 0 \\ d_{15} & d_{15} & d_{33} & 0 & 0 & 0 \end{bmatrix} \begin{pmatrix} E_x^2 \\ E_y^2 \\ E_z^2 \\ 2E_y E_z \\ 2E_x E_z \\ 2E_x E_y \end{pmatrix} = E_0^2 \begin{pmatrix} -2d_{15} \sin\theta \cos\theta \\ 0 \\ d_{31} \sin^2\theta + d_{33} \cos^2\theta \end{pmatrix}.$$

And our experimental configuration collects in-plane electric field components of SHG light as follows:

$$I_x^{2\omega} \propto |\mathbf{P} \cdot \mathbf{A}_x|^2 \propto |d_{31} \sin^2\theta + d_{33} \cos^2\theta|^2$$

$$I_y^{2\omega} \propto |\mathbf{P} \cdot \mathbf{A}_y|^2 \propto |2d_{15} \sin\theta \cos\theta|^2$$

where \mathbf{A}_i corresponds to the orientation of the output analyzer in position i (expressed, $\mathbf{A}_x = (0, 0, 1)$ and $\mathbf{A}_y = (0, 0, 1)$). The SHG experimental setup does not use a polarizer; therefore, the total SHG emission measured by its configuration is $I_x^{2\omega} + I_y^{2\omega}$. The non-zero d_{ij} components indicate that in-plane polarized regions of this thin film can produce non-zero SHG light captured by this measurement configuration.

Meanwhile, for out-of-plane polarization, the electric field of fundamental light has components $\mathbf{E}^\omega(\theta) = (E_0 \cos\theta, -E_0 \sin\theta, 0)$. Then, the nonlinear polarization is

$$\mathbf{P} = E_0^2 \begin{pmatrix} 0 \\ 0 \\ d_{31} \cos^2\theta + d_{32} \sin^2\theta \end{pmatrix}.$$

Applying $\mathbf{A}_x = (1, 0, 0)$ and $\mathbf{A}_y = (0, 1, 0)$, both $I_x^{2\omega}$ and $I_y^{2\omega}$ become zero.

Thus, this result indicates that our SHG measurement configuration is exclusively sensitive to in-plane polarizability of the Pca2₁ structure ($2mm$ point group). Indeed, an in-plane projection of the polarization is expected in the ultrathin ferroelectric ZrO₂ films based on its predominant orientation (fig. S3, Main Text).

Regarding the nonpolar P4₂/nmc tetragonal phase (*4/m* point group) present in thicker ZrO₂ films, the piezoelectric matrix is empty; therefore, no light-induced nonlinear polarization is expected for these nonpolar structures.

Electrical Analysis

Dielectric permittivity extraction from MOS capacitors The permittivity of ZrO₂ was extracted from thickness-dependence MOS *C-V* measurements (fig. S9) on lightly-doped p-type substrates. In the accumulation region of the MOS *C-V* measurements, the MOS capacitor can be modelled as three capacitors (ZrO₂ layer, SiO₂ layer, and Si space charge layer) in series using the following equation,

$$\frac{1}{C} = \frac{1}{\epsilon_0 \epsilon_{ZrO_2}} t_{ZrO_2} + \frac{1}{\epsilon_0 \epsilon_{SiO_2}} \left[t_{SiO_2}^{phys} + \frac{t_{CL} \epsilon_{SiO_2}}{\epsilon_{Si}} \right]$$

where t_{ZrO_2} is the thickness of the ZrO₂ layer, $t_{SiO_2}^{phys}$, is the physical SiO₂ thickness, and t_{CL} is the charge layer thickness in silicon. The physical SiO₂ thickness is constant across all ZrO₂ film thicknesses. Additionally, the capacitance values were extracted at a fixed charge of $Q = -1 \mu\text{C}/\text{cm}^2$ which ensures that the charge-layer thickness is constant across all thicknesses and in the accumulation region. Therefore, from Equation 3, the inverse capacitance at a fixed charge as a function of ZrO₂ thickness should result in a line and the permittivity of the ZrO₂ layer can be extracted from the slope.

Polarization switching via tunnel junctions *I-V* measurements in tunnel junctions overcome shortcomings faced by conventional ferroelectric *P-V* and *C-V*, piezoresponse, and synchrotron X-ray techniques by leveraging tunnel currents, disentangling competing hysteretic mechanisms, and demonstrating polarization switching, respectively. For example, hysteresis loops from polarization-voltage (*P-V*) and capacitance-voltage (*C-V*) measurements – the traditionally-demonstrated smoking-gun evidence of polarization switching – become obsolete in the ultrathin regime once leakage currents dominate switching current and distort the extracted behavior (69). Meanwhile, tunnel junctions exploit the tunnel current via its polarization-dependence, allowing for ferroelectric measurements in the sub-5 nm regime. Tunnel junctions *I-V* measurements also overcome the key limitation of synchrotron X-ray characterization, which can bypass leakage to examine polar symmetry in ultrathin films, but fail to demonstrate polarization switching (70,71). Piezoresponse measurements can also eliminate leakage and demonstrate polarization switching, but its electrically-modulated tip deflection can be confounded by various electrochemical, electromechanical, and electrostatic artefacts which can give rise to hysteretic piezoresponse (42,72). Therefore, characterizing ultrathin ferroics via tunnel junctions (Fig. 3C, fig. S14) present a complementary *I-V* methodology for disentangling confounding hysteretic mechanisms from polarization switching, serving as a promising metrology tool for advanced nanoelectronics (73) in tandem with scanning probe microscopy (74). Indeed, *I-V* measurements have been previously employed to demonstrate ultrafast polarization switching in thicker ALD-grown HfO₂-ZrO₂ thin films (75–79). Furthermore, in other ferroelectric material systems, FTJ *I-V* measurements have been used to pinpoint ferroelectric origins in both ultrathin oxides (80, 81) and emerging two-dimensional systems exhibiting hysteretic resistive switching (82).

Distinguishing polarization switching via electrical measurements It is worth noting that oxygen-vacancy-based contributions can be intertwined with polarization switching in oxide

ferroelectrics; indeed, some degree of influence of electrochemical phenomena intertwined with ferroelectric polarization switching has been observed for both perovskite-based (83–88) and fluorite-based (19, 89–93) FTJs. In particular, voltage-driven oxygen vacancy migration is the commonly employed resistive switching mechanism in resistive random access memories (RRAMs) (94,95), in which oxygen vacancies form conductive-filaments within the dielectric barrier layer. Therefore, to examine potentially confounding ionic and electrochemical contributions in the ultrathin ZrO₂ FTJs, further I - V measurements were performed.

In particular, voltage polarity-dependent pulsed I - V_{write} hysteresis measurements (fig. S14D) are able to rule out filamentary-type resistive switching mediated by electrochemical ionic-driven mechanisms. For typical bipolar filamentary-mediated resistive switching, the filament formation set by the first polarity results in the high-current state; therefore, the sense of hysteresis is dependent on the direction of the voltage sweep (96). Meanwhile, for polarization-mediated switching, the polarization-induced band modulation sets the current states; the polarization direction in the ferroelectric barrier is set by the polarity of the voltage pulse, independent of the sweep direction. Therefore, for polarization-driven switching, the same I - V_{write} hysteresis sense should be observed independent of the sweep direction, consistent with the behavior observed in the ultrathin ZrO₂ FTJs (fig. S14D). Additionally, the measured pulsed- I - V hysteresis loops for ultrathin ZrO₂ (Fig. 3C, fig. S14D), which shows two stable resistance states – corresponding to the two remnant polarization states – match piezoresponse hysteresis loops (fig. S14C), also strongly suggestive of polarization-driven switching (97). Furthermore, the observed counter-clockwise hysteresis sense (Fig. 3C, fig. S14D) is consistent with polarization-induced barrier height modulation as depicted in the electron band diagrams (fig. S14E) – positive voltage applied to the top electrode results in a lower average barrier height, and therefore, operates as the high current state. Moreover, the presence of closed hysteresis loops likely preclude ionic-driven mechanisms, which have been shown to result in open resistive hysteresis loops in HfO₂-based junctions (89, 92), likely due to irreversible oxygen vacancy migration. The lack of a forming step at high voltage required to observe resistive hysteretic switching also renders ionic-driven filamentary-based mechanisms unlikely.

All of the aforementioned behaviors to eliminate effects related to charge injection and demonstrate polarization-driven resistive switching have been established in previous works on similar ultrathin FTJs integrating ALD-grown 1 nm Zr:HfO₂ barriers on SiO₂-buffered Si (11,23). Therefore, although the co-existing, and often synergistic (19,89) influence of various electrochemical and ionic phenomena intertwined with polarization switching cannot be completely eliminated, multiple I - V signatures in these ultrathin ZrO₂ FTJs indicate minimal contributions from various ionic-driven mechanisms and indicate the observed resistive switching behavior is consistent with ferroelectric polarization switching.

Such charge injection concerns are even less likely for the in-plane IDE P - V measurements (Fig. 3, fig. S10,15) considering IDE structures ($\sim 1 \mu\text{m}$ oxide barrier) possess significantly lower leakage current compared to that present in out-of-plane tunnel junctions ($\sim 1 \text{ nm}$ oxide barrier).

Distinguishing polarization switching via scanning probe microscopy Regarding scanning probe microscopy (SPM) images (fig. S13), measures were taken to eliminate non-polarization-driven mechanisms of PFM contrast. AFM topography images before and after voltage poling ultrathin (0.5 nm, 1 nm) ZrO₂ films demonstrate no surface morphology changes to the films due to poling (fig. S13A,B), which indicate the strong PFM amplitude and phase contrast in ultrathin

ZrO₂ present after poling (fig. S13 C,D) are not artifacts from charge injection or other electrochemical origins. This also rules the possibility of cross-talk between topography and phase retraces leading to false phase contrast. Furthermore, PFM phase contrast for ultrathin (0.5 nm, 1 nm) ZrO₂ films persists after 2 hours; such long-term retention significantly suppresses shorter-scale effects such as charge injection, further suggesting that the PFM contrast is due to ferroelectric polarization behavior. Furthermore, the presence of spontaneous as-grown polarization further indicates that the observed PFM contrast upon voltage application is inherent to the film's polar nature, and not an extrinsic tip-induced artifact.

Origin of as-grown spontaneous polarization Notably, unpoled regions of ultrathin (0.5, 1 nm) ZrO₂ films demonstrate the same PFM phase contrast as positively poled regions (fig. S13D), indicating that ultrathin ZrO₂ exhibits spontaneous polarization. Regarding the origin of this spontaneous polarization, the spectroscopic signatures of ultrathin-enhanced polar distortion (Fig. 2) indicate the presence of a polarization and the highly-oriented nature of the ultrathin films (fig. S3) requires the presence of an out-of-plane (OOP) projection of the Pca2₁ polar axis; therefore, this OOP polarization would be detected by the PFM measurement. These reasons establish why a spontaneous OOP polarization is expected to be present. To explain why one polarization state over the other is preferred, the nature of the SiO₂/ZrO₂ interface must be considered. The high- κ oxide and semiconductor device community has extensively characterized interface traps states (D_{it}) at SiO₂-HfO₂ and SiO₂-ZrO₂ interfaces, inherent to low-temperature ALD deposition on amorphous (SiO₂) templates; these states can serve as bound charges at the interface, which would in turn, prefer a specific (up or down) polarization state. The preferred polarization in ultrathin (0.5, 1 nm) ZrO₂ films points toward silicon, consistent with negatively charged bound charges at the SiO₂-ZrO₂ interface.

Fluorite-Structure Ferroelectric Considerations

ZrO₂ versus HfO₂ To help unravel these curious size effects, key fluorite-structure insights can be derived from the competing symmetries inherent to its rich polymorphic nature (15), particularly surface energy (98) contributions. Thermodynamic (99,100) and kinetic (99) contributions help explain why ZrO₂ is preferred to its sister fluorite-structure binary oxide HfO₂ for stabilizing the ferroelectric o-phase in the ultrathin regime. In particular, the low temperature of crystallization for ZrO₂ relative to HfO₂ (101) eliminates potential reversion back to the bulk-stable paraelectric monoclinic formation, which has been observed upon cooling after the typical high-temperature post-deposition annealing usually required for phase crystallization in HfO₂-based thin films (102). Crystallizing ZrO₂ at low temperatures during the ALD deposition itself avoids such kinetic effects (99), which allows dimensionality-driven size effects (discussed in Main Text) to maintain as the major energy driving force, thereby keeping the metastable ferroelectric o-phase trapped.

Fluorite-structure antiferroelectricity We note here that the original Kittel view of an "antipolar" crystal structure with two sublattices of opposite polarization (103) does not seem to apply to the nonpolar $P4_2/nmc$ tetragonal lattice attributed to fluorite-structure antiferroelectricity (104). Instead, the more inclusive definition of antiferroelectricity put forth in recent years (105) – i.e. reversible field-dependent first-order nonpolar-to-polar phase transition without explicitly requiring an anti-polar phase – more accurately describes this fluorite-structure system. The

expected field-induced nonpolar-to-polar (tetragonal $P4_2/nmc$ to orthorhombic $Pca2_1$) phase transition for fluorite-structure antiferroelectrics (104) was first theoretically established (24) and later experimentally demonstrated via field-dependent diffraction (106), electron microscopy (107,108), scanning probe microscopy (61) and electrical measurements (109) in Hf:ZrO₂ and ZrO₂ thin films. In this work, the relatively thick ZrO₂ films indeed index to the nonpolar tetragonal $P4_2/nmc$ (Fig. 1, S4, S5, S8) and exhibit the characteristic antiferroelectric-like double-hysteresis behavior (Fig. 3B, E); therefore, our results are consistent with the more recent picture of antiferroelectricity (105) – i.e. field-induced ferroelectric state – that has been ascribed to the HfO₂-ZrO₂ family (104).

The distinguishing feature of this work is we instead focus on the thickness-driven – rather than field-driven – nonpolar t-phase to polar o-phase transition driven by reduced dimensionality in ZrO₂ thin films. Original studies into fluorite-structure systems examined the ferroelectric-antiferroelectric phase competition as a function of temperature and composition in thick (> 10 nm) films (4,110–112). More recent studies have examined antiferroelectricity down to the 4-5 nm regime in ALD-grown Hf:ZrO₂ (76) and ZrO₂ (58,61,113,114), but to date, the ultrathin (< 2 nm) regime has yet to be examined for fluorite-structure antiferroelectrics. Therefore, the size-driven antiferroelectric-to-ferroelectric phase transition has yet to be observed due to the unconventional size effects intrinsic to fluorite-structure ferroelectrics (discussed in Main Text), e.g. the sensitivity of t-phase and o-phase relative free energies to reduced size and surface energy effects (21,115).

Depolarization field considerations Besides the unique piezoelectric origins, unconventional ferroelectric origins have also been attributed to the fluorite-structure binary oxides (12,13). First-principles calculations suggest improper origins (12) may facilitate the persistence of atomic-scale ferroelectricity, as 2D fluorite-structure $Pca2_1$ layers have minimal depolarizing field associated with its structure, enabling unsuppressed polarization down to the u.c. thickness limit (12,13). Depolarization fields are the electrostatic penalty for electric dipoles at the ultrathin scale; accordingly, ferroelectricity in conventional perovskite oxides is typically suppressed at the few nanometer scale (29), as metals with finite screening cannot completely compensate the surface dipole charges (2). The ultrathin o-ZrO₂ films in this work are able to overcome depolarization effects, which would otherwise prohibit sustained polarization in the atomic-scale regime, due to its in-plane polarization, as evidenced by SHG mapping (Fig. 2C) and in-plane polarization switching (Fig. 3). For these films, the dominant out-of-plane orientation is the (111) (fig. S3); this close-packed plane is expected to be favored in the ultrathin regime due to the enhanced importance of surface energies at reduced dimensions. Considering the polar axis for the $Pca2_1$ structure is along a principal lattice direction, o-ZrO₂ films demonstrate a significant in-plane polarization component. Therefore, the highly-oriented nature of the ultrathin ZrO₂ films also contribute to the sustained atomic-scale electric polarization. In fact, van der Waals (vdW) chalcogenides have recently emerged to overcome ultrathin ferroelectric limitations via in-plane polarization (116); for perovskite-based ferroelectrics, exploiting epitaxial strain to stabilize in-plane polarization (117) could similarly help bypass these depolarization concerns in the ultrathin regime. Furthermore, the improper origin of fluorite-structure ferroelectricity (12,13) helps make it secondary polar distortion impervious to depolarization effects (28).

System	Material	Thickness (Å)	Dipole	Polarization switching?	Ref.
vdW	h-BN	6.6	OOP	BL: I - V loop, PFM loop	(118,119)
vdW	Graphene	6.7	OOP	BL: I - V loop	(120)
vdW	SnTe	6*(12)	IP	*ML: no (BL: I - V loop)	(121)
vdW	SnS	6	IP	ML: I - V loop	(122)
vdW	MoTe ₂	8	OOP	ML: PFM loop, no I - V	(82)
vdW	WTe ₂	14	OOP	BL: I - V loop	(123)
vdW	In ₂ Se ₃	12	OOP/IP	ML: PFM loop	(124)
vdW	BA ₂ PbCl ₄	17*	IP	*No switching loops	(125)
vdW	CuInP ₂ S ₆	40	OOP	PFM loop	(126)
Polymer	P(VDF-TrFE)	10	OOP	BL: I - V loop (Pyro)	(127)
Perovskite	BaTiO ₃	10*	OOP	*2-3 uc: No switching loop	(81)
Perovskite	PbTiO ₃	12*	OOP	*3 uc: No switching loop	(70)
Perovskite	BiFeO ₃	4*(8)	OOP	*1 uc: No (2 uc: PFM loop)	(80)
Perovskite	BiFeO ₃	8	OOP	2 uc: PFM loop, no I - V	(128)
Perovskite	Pb(Zr,Ti)O ₃	6*	OOP	*1.5 uc: No	(129)
Fluorite	Zr:HfO ₂	25	OOP	PFM loops	(130)
Fluorite	Zr:HfO ₂	< 20	OOP	PFM loops	(131)
Fluorite	Zr:HfO ₂	15	OOP	P - V loops	(132)
Fluorite	Zr:HfO ₂	15*(50)	OOP	*No switching (P - V loops)	(10)
Fluorite	Zr:HfO ₂	10	OOP	C - V & I - V loops	(11,23)
Fluorite	ZrO ₂	5-6	OOP/IP	P - V & I - V loops	this work

Table S1. Atomic-scale demonstrations of ferroelectricity. Note some works prove inversion symmetry-breaking, but do not demonstrate hysteretic polarization switching (indicated by "*" symbols). Abbreviations: van der Waals (vdW); out-of plane (OOP); in-plane (IP); current-voltage (I - V); capacitance-voltage (C - V); polarization-voltage (P - V); unit cell (uc); monolayer (ML); bilayer (BL).

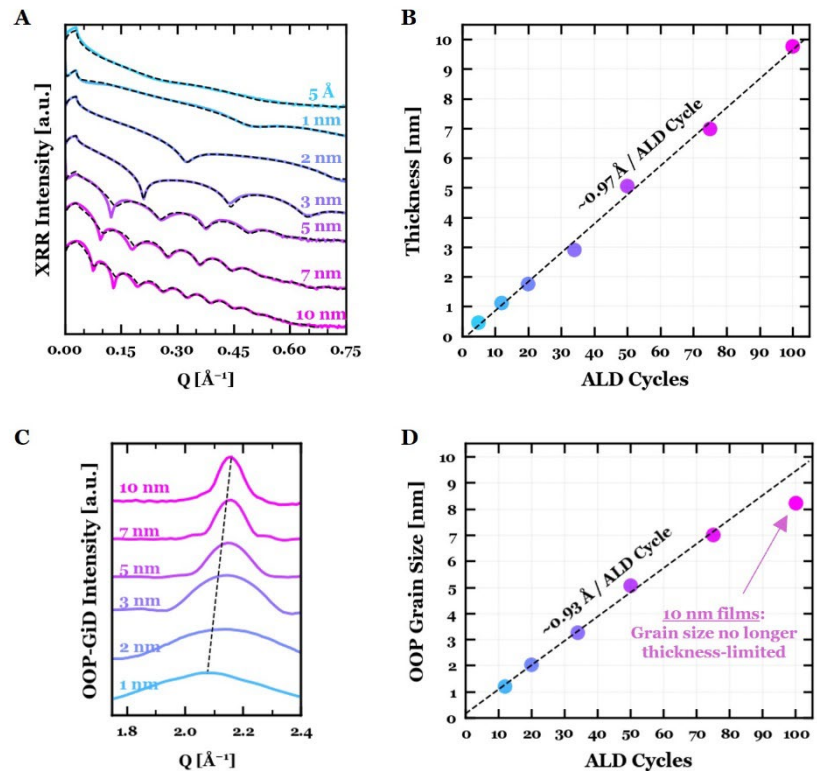


Fig. S1. Thickness verification of ALD-grown ZrO₂ via X-ray analysis. (A) Synchrotron X-ray reflectivity (XRR) of the ZrO₂ thickness series from 10 nm down to 0.5 nm thickness. The dotted black lines overlaid on the data are XRR simulations from which the thickness values reported in panel (B) are determined. (B) The extracted growth rate (~ 10 ALD cycles $\equiv 1$ nm thickness) is consistent with Zr:HfO₂ films extensively characterized in previous work on ultrathin Zr:HfO₂ films (11). (C) Out-of-plane grazing incidence diffraction (OOP-GiD) of the ZrO₂ thickness series. (D) Extracted growth rate from the OOP-GiD grain size analysis (Supplementary Text). Note for 10 nm (100 ALD cycles) films, the grain size is no longer limited by the thickness of the film, so this data point is not used for the thickness analysis.

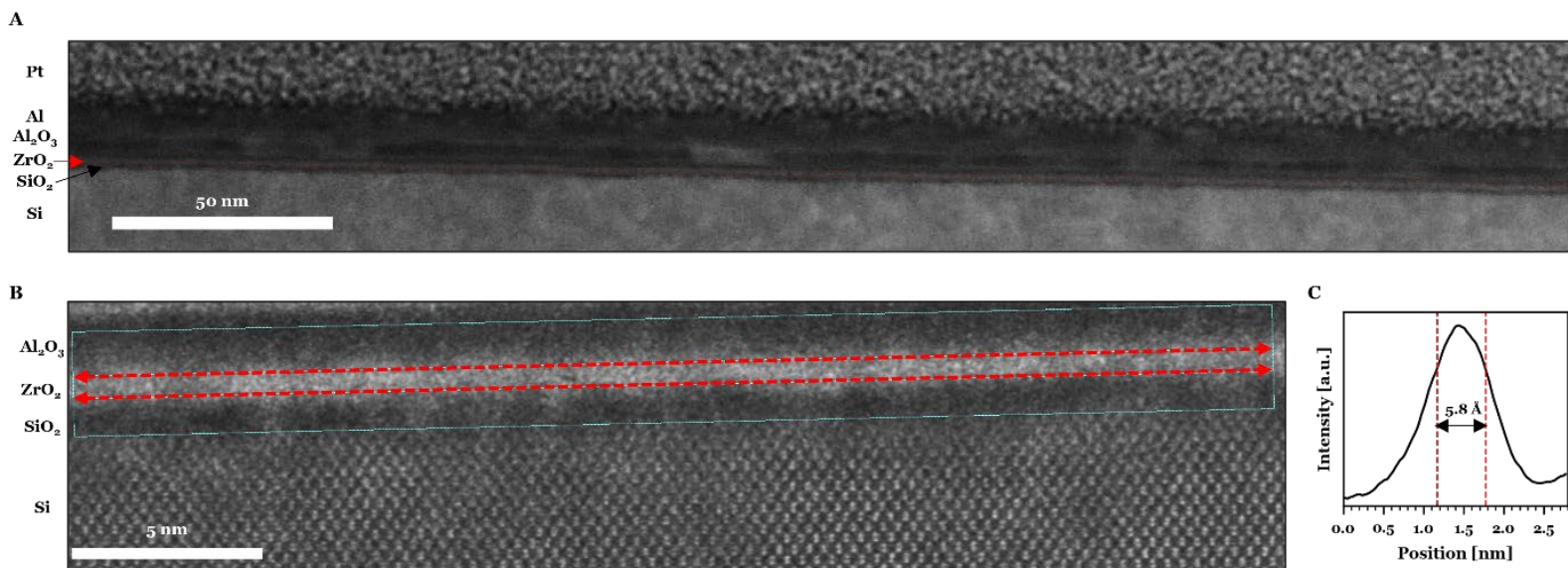


Fig. S2. Thickness verification of ALD-grown ZrO₂ via TEM analysis. **(A)** Wide field-of-view (FoV) HAADF-STEM image for a 5 ALD cycle ZrO₂ thin film on SiO₂-buffered silicon substrate illustrating the wide-area stability of ultrathin ZrO₂ layer (lighter contrast layer delineated by the faint red dotted lines) across ~ 350 nm FoV. **(B)** Zoomed-in HAADF-STEM image of the ultrathin ZrO₂ film from (A). **(C)** The ZrO₂ layer thickness is determined by line profile analysis. The ZrO₂ film (light contrast) examined here is capped with Al₂O₃ (dark contrast) to provide maximize Z-contrast in the dark field imaging mode to aid in layer delineation. The red boundary lines are determined by eye based on the color contrast. The blurred interfaces inherent to non-epitaxial ALD-grown films on amorphous underlayers (SiO₂) and capped with amorphous top layers (Al₂O₃) complicates TEM-based thickness extraction; therefore, X-ray based methodologies (fig. S1) are preferred for ultrathin thickness determination (Supplementary Text). Nonetheless, the extracted thickness of ~ 0.58 nm is close to the ~ 0.5 nm thickness determined from X-ray based techniques (fig. S1) for 5 ALD cycle ZrO₂ films.

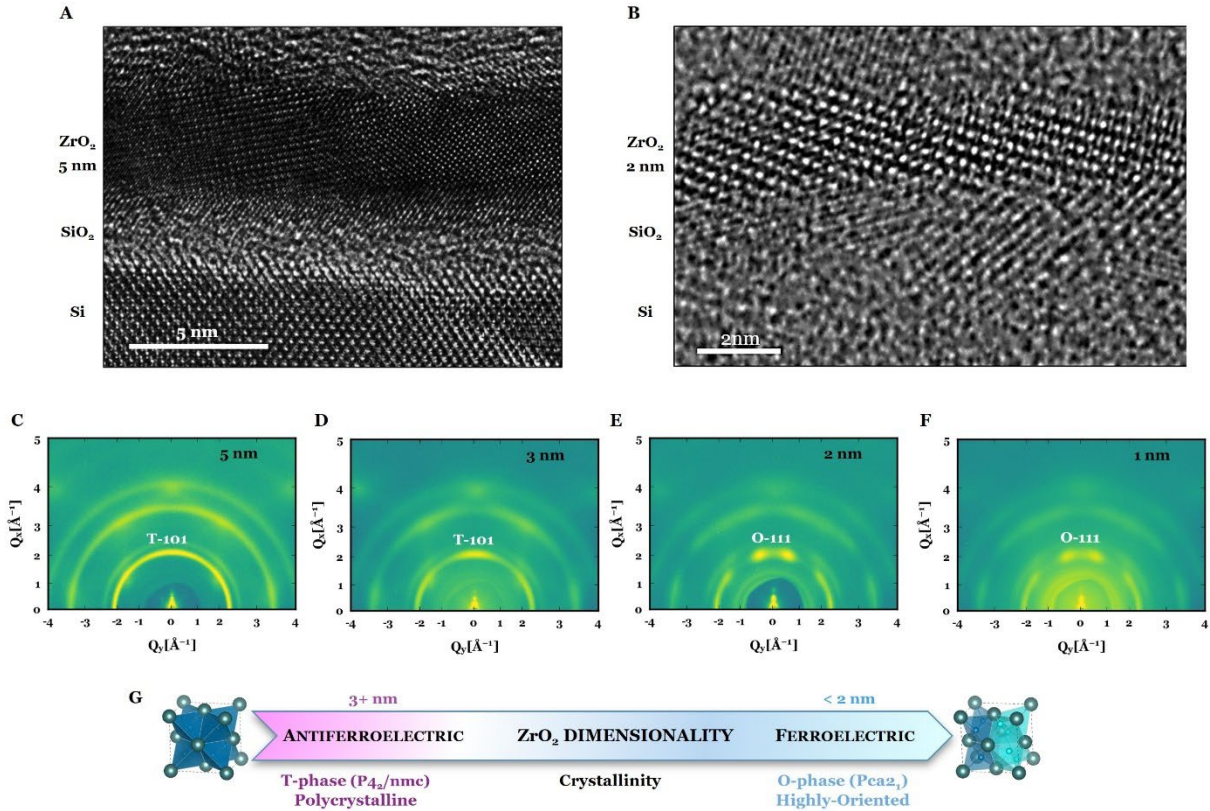


Fig. S3. Crystalline ultrathin ZrO₂ films. (A,B) Wide field-of-view cross-sectional TEM images of 5 nm (A) and 2 nm (B) ZrO₂ on SiO₂-buffered Si, used for the phase identification analysis (Fig. 1D-G) based on HR-TEM simulations (fig. S5). Note the Si substrate is tilted off its zone axis to image the crystallinity present more clearly in the 2 nm ZrO₂ layer. (C,D,E,F) 2D RSMs for 5 nm (C), 3 nm (D), 2 nm (E), and 1 nm (F) ZrO₂ on SiO₂-buffered Si, demonstrating the presence of crystalline films. Furthermore, the 2D maps indicate the emergence of enhanced texturing in ultrathin films (≤ 3 nm) – consistent with previous work on ALD-grown ultrathin Zr:HfO₂ films (11, 131) – illustrated by concentrated intensity spots rather than polycrystalline rings. The integrated 1D spectra also are consistent with the $P4_2/nmc$ and $Pca2_1$ indexing in thick and ultrathin films, respectively; in particular, the splitting of the reflection around $Q_x \sim 2 \text{ \AA}^{-1}$ for films ≤ 2 nm suggests a symmetry-lowering transition from the $P4_2/nmc$ T-phase, consistent with the $Pca2_1$ O-phase. However, we note that the IP-GiD spectra (fig. S4) are used for more rigorous indexing analysis to the respective phases (Materials and Methods). These qualitative 2D diffraction maps are primarily meant to highlight the highly-oriented crystalline nature of the ultrathin ZrO₂ films. (G) Dimensionality-driven evolution of ZrO₂ from the antiferroelectric tetragonal phase to the ferroelectric orthorhombic phase illustrated through qualitative crystallinity features.

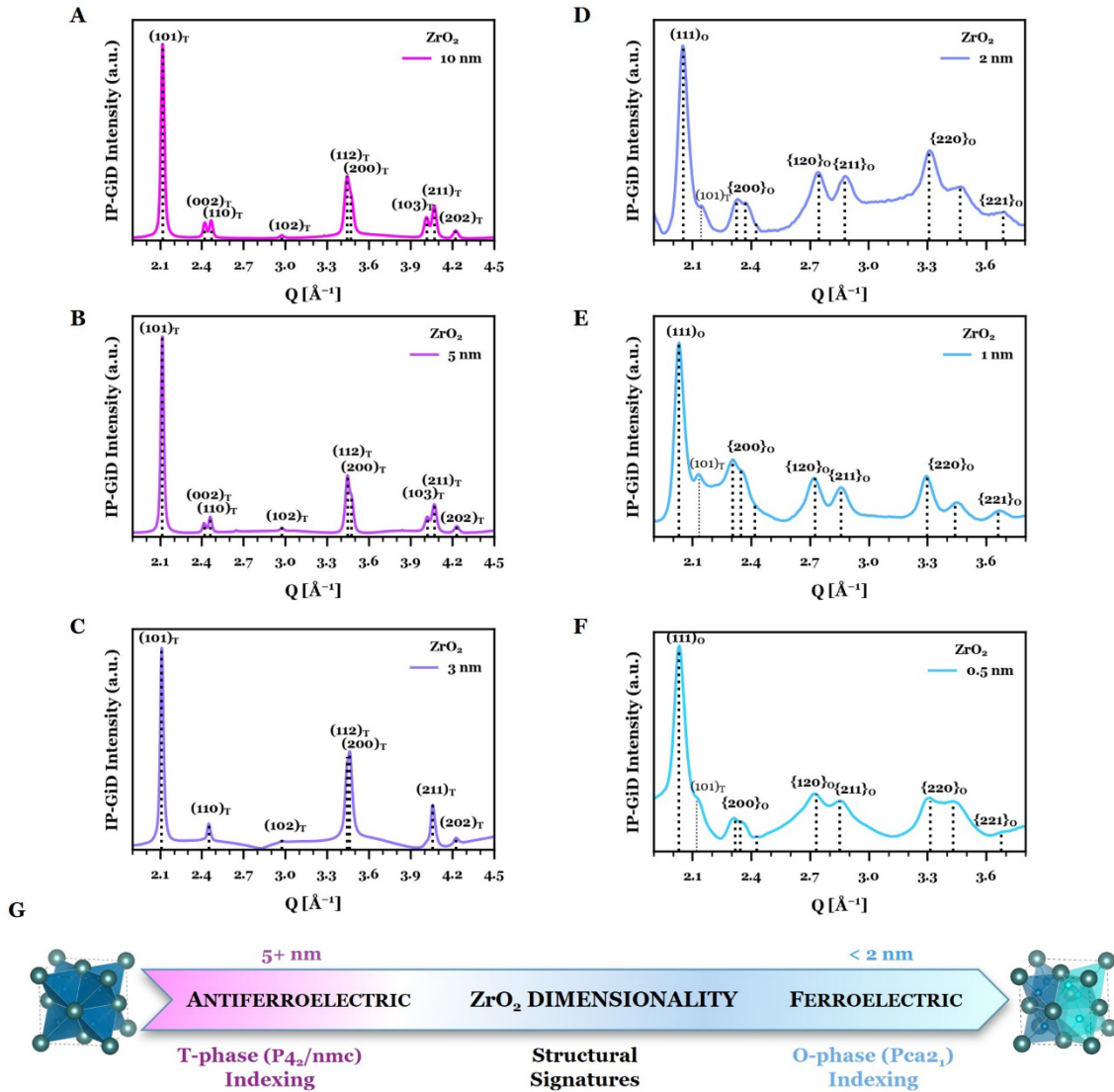


Fig. S4. Ferroic phase identification from synchrotron X-ray diffraction. (A,B,C,D,E,F) Synchrotron in-plane grazing incidence diffraction (IP-GiD) for the ZrO₂ thickness series in the relatively thick (10 nm, 5 nm, 3 nm) and ultrathin (2 nm, 1 nm, 5 Å) regime. In-plane GiD indicates the presence of the antiferroelectric t-phase in relatively thick (> 2 nm) ZrO₂ films, while in-plane GiD indicates an emergence of the ferroelectric o-phase for ZrO₂ films below 2 nm. 2 nm ZrO₂ marks the critical thickness for the symmetry-lowering tetragonal-to-orthorhombic structural phase transition, as illustrated by the increased number of reflections in ultrathin films, some of which are forbidden in the higher-symmetry t-phase. The detailed self-consistent indexing analysis considering multiple reflections is described in the Supplementary Text. (G) Dimensionality-driven evolution of ZrO₂ from the antiferroelectric tetragonal phase to the ferroelectric orthorhombic phase demonstrated through structural signatures from diffraction.

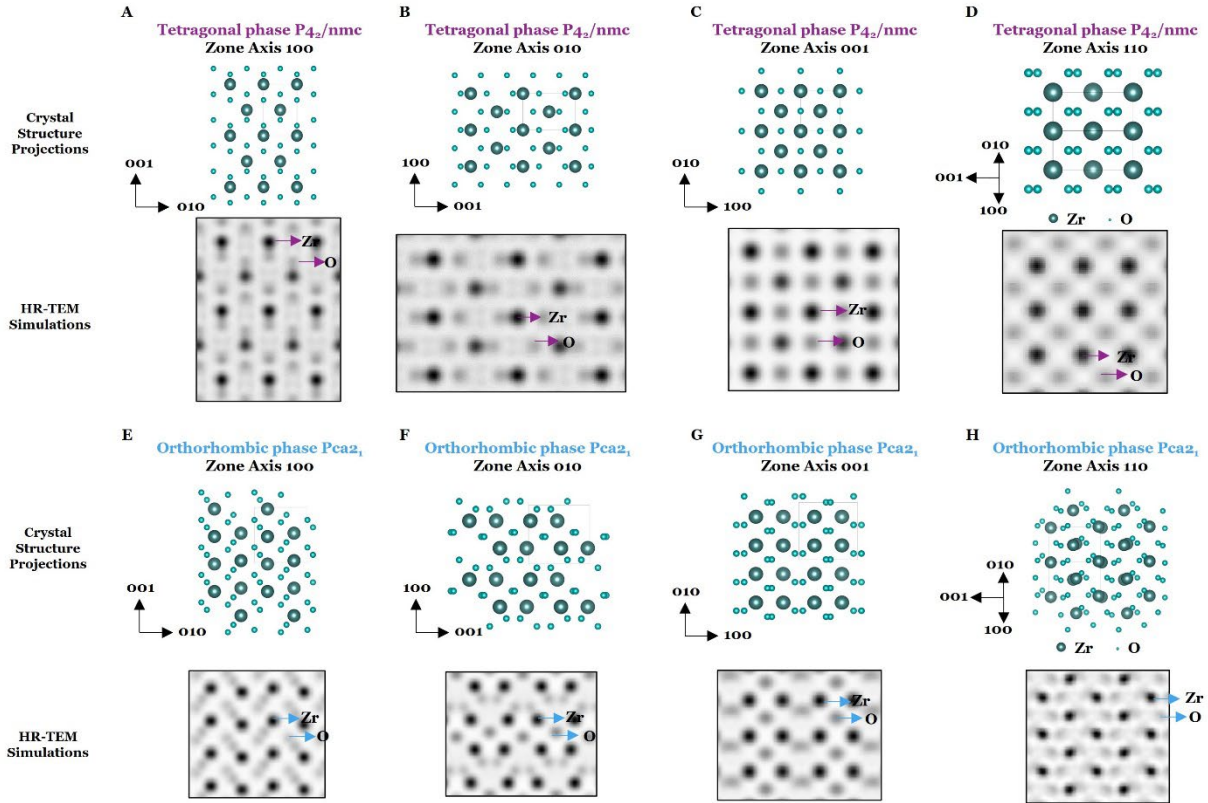


Fig. S5. Ferroic phase identification from oxygen imaging analysis. (A,B,C,D) Crystal structure projections (top) and HR-TEM simulations (bottom) along the 100 (A), 010 (B), 001 (C), and 110 (D) zone axes for the tetragonal $P4_2/nmc$ structure. The experimental HR-TEM imaging of 5 nm ZrO_2 (Fig. 1D,E) matches with the [001] projection of crystal structure and TEM simulation for the tetragonal $P4_2/nmc$ structure. (E,F,G,H) Crystal structure projections (top) and HR-TEM simulations (bottom) along the 100 (E), 010 (F), 001 (G), and 110 (H) zone axes for the orthorhombic $Pca2_1$ structure. The experimental HR-TEM imaging of 2 nm ZrO_2 (Fig. 1F,G) matches with the [110] projection of crystal structure and TEM simulation for the orthorhombic $Pca2_1$ structure. Note all HR-TEM simulations are provided in inverted contrast to better accentuate the oxygen atoms under the following conditions: specimen thickness ~ 10 nm and defocus = 4 nm (Materials and Methods).

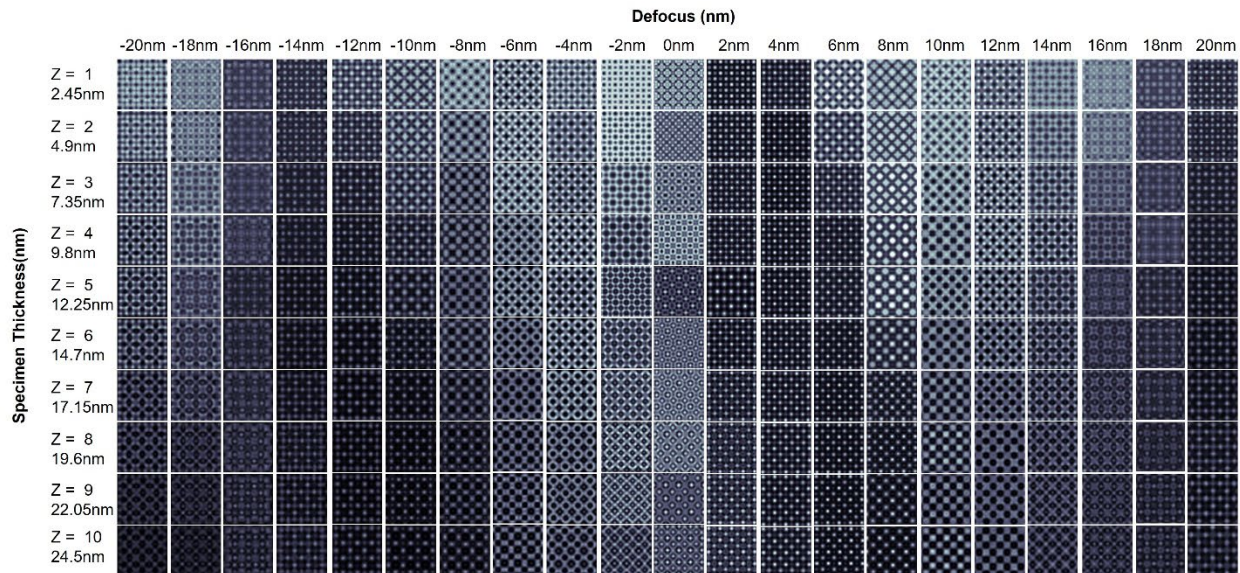


Fig. S6. Determining oxygen imaging conditions from HR-TEM simulations. Tetragonal $P4_2/nmc$ ZrO_2 HR-TEM simulations as a function of defocus value and TEM specimen thickness under the following experimental conditions: $C_s = -16 \mu\text{m}$, $C_5 = 6.8 \text{ mm}$, slice thickness = 20 \AA , and 300 kV accelerating voltage. The simulations indicate that the oxygen atoms become visible at appropriate defocus values (~ 2 to 4 nm) and reasonable specimen thicknesses (below 12.25 nm), which is similar to the experimental oxygen imaging conditions (Materials and Methods).

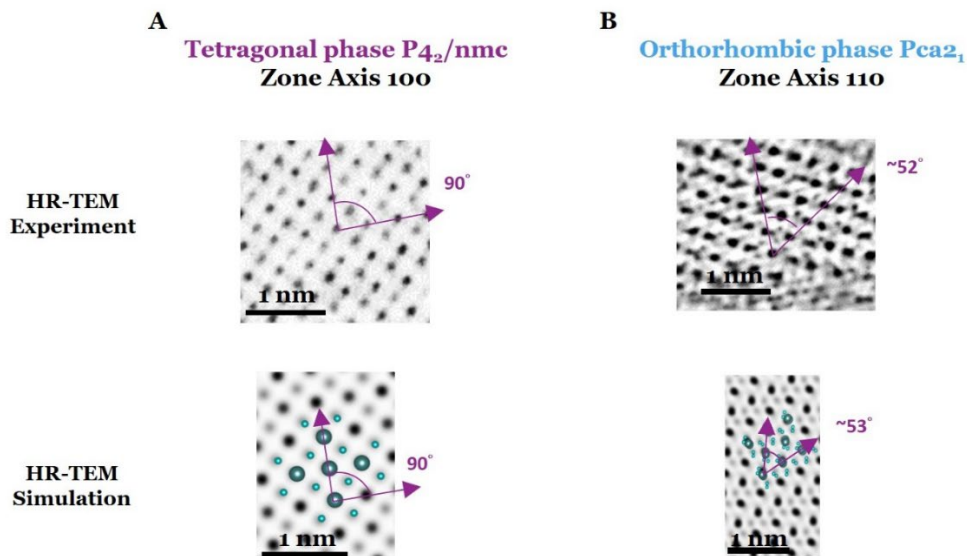


Fig. S7. Ferroic phase identification from lattice angle analysis. (A) Experimental HR-TEM imaging of 5 nm ZrO_2 (top) matches the expected cation-cation bond angle along the [001] projection of the tetragonal $P4_2/nmc$ structure (bottom). (B) Experimental HR-TEM imaging of 2 nm ZrO_2 (top) matches the expected cation-cation bond angle along the [110] projection of the orthorhombic $Pca2_1$ structure (bottom). The slight angle deviation may be possibly due to distorted regions present in the thin sample specimen. The simulations in (A) and (B) implemented the following conditions: specimen thickness ~ 9.8 nm and defocus = 4 nm (Materials and Methods).

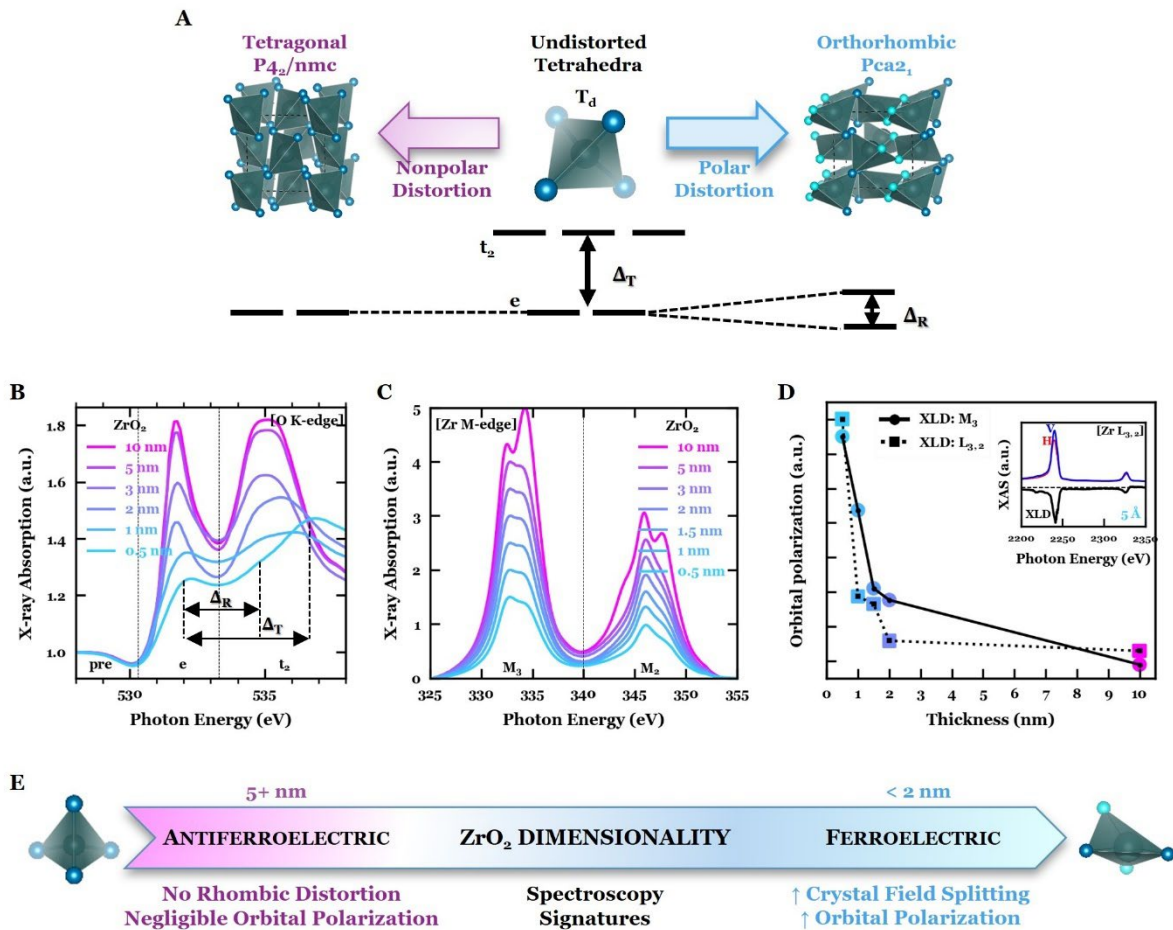


Fig. S8. Ferroic phase insights from synchrotron X-ray spectroscopy. (A) Crystal field splitting diagram for tetragonal and orthorhombic phases. Symmetry-induced e -manifold splitting can provide a spectroscopic signature of polar orthorhombic phase (Supplementary Text). (B) Thickness dependent XAS spectra at the oxygen K -edge, indicating the pronounced presence of the polar rhombic distortion, indicative of the ferroelectric o-phase, in ultrathin ZrO_2 films. (C) Thickness-dependent XAS spectra at the Zr $M_{3,2}$ -edge; the crystal field features present underlie the presence of crystalline ZrO_2 films down to the atomic-scale limit. (D) Extracted orbital polarization – indicative of polarization (Supplementary Text) – from XLD measurements at the Zr $M_{3,2}$ -edge and Zr $L_{3,2}$ -edge as a function of ZrO_2 thickness; the ultrathin-enhanced orbital polarization is likely due to the increased ferroelectric phase emergence and polar distortion present in thinner ZrO_2 films (Fig. 1, 2). Inset: linear polarization-dependent XAS (red, blue) and XLD (black) of 5 Å ZrO_2 at the Zr- $L_{3,2}$ -edge. (E) Dimensionality-driven evolution of ZrO_2 from the antiferroelectric tetragonal phase to the ferroelectric orthorhombic phase demonstrated through structural signatures in X-ray spectroscopy.

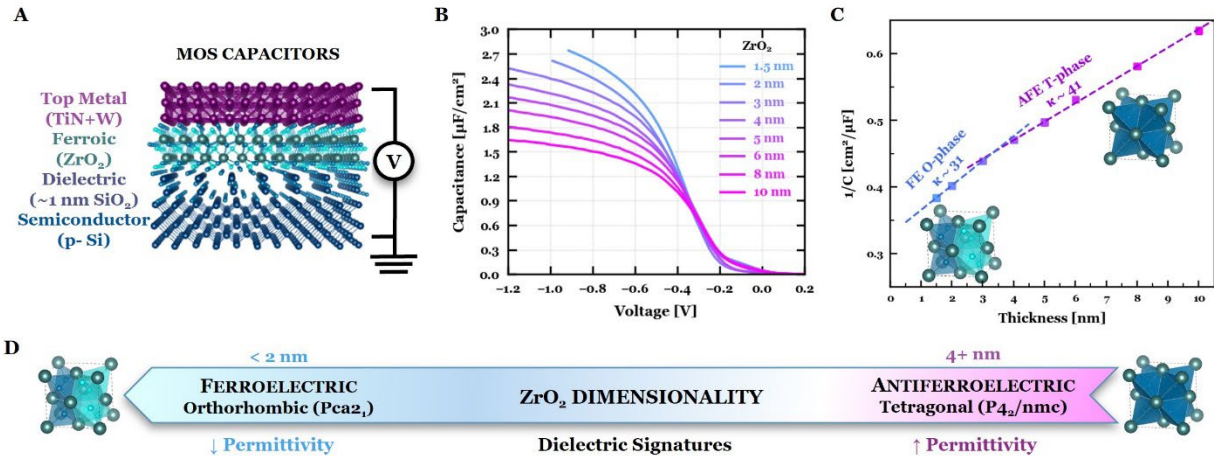


Fig. S9. Ferroic phase insights from dielectric measurements. (A) Schematic of MOS capacitors used for accumulation C - V measurements. (B) C - V measurements of ZrO₂ thickness series in MOS capacitors. (C) Extracted permittivity (κ) from ZrO₂ thickness-dependent MOS C - V measurements. The extracted permittivity crosses over from antiferroelectric t-phase permittivity in relatively thick regime (4+ nm) – $\kappa \sim 40$ (4) – towards more ferroelectric-like o-phase permittivity – $\kappa \sim 30$ (4,21) – for ultrathin ZrO₂ films. (D) Dimensionality-driven evolution of ZrO₂ from the antiferroelectric tetragonal phase to the ferroelectric orthorhombic phase demonstrated through dielectric measurements.

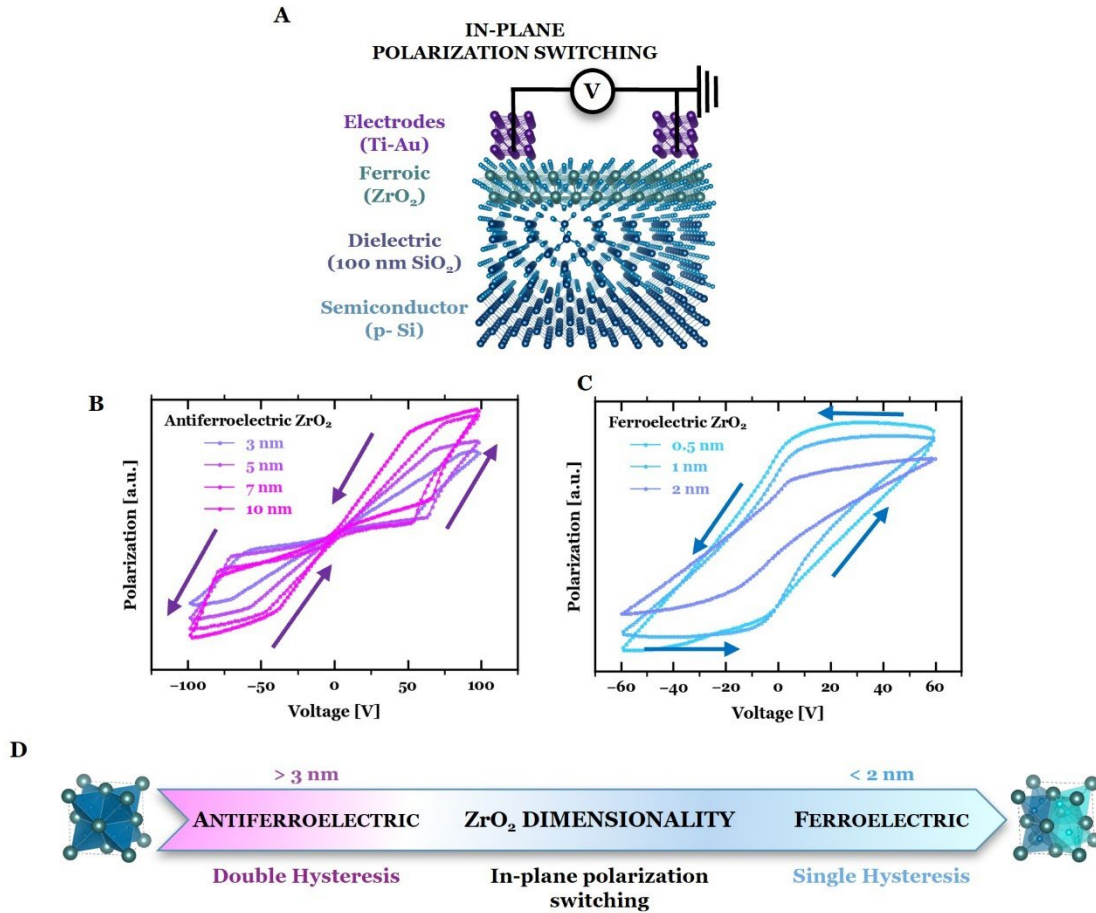


Fig. S10. Ferroic phase insights from in-plane polarization-voltage loops. (A) Schematic of the in-plane device structures used for in-plane polarization-voltage (P - V) loops. (B) Antiferroelectric-like counter-clockwise double hysteresis P - V behavior for relatively thick (3, 5, 7, 10 nm) ZrO_2 . (C) Ferroelectric-like counter-clockwise hysteresis P - V behavior for ultrathin (2, 1, 0.5 nm) ZrO_2 films. Note the slightly pinched P - V behavior for 2 nm ZrO_2 is consistent with the structural trends indicating 2 nm is around the AFE-to-FE phase transition point. (D) Dimensionality-driven evolution of ZrO_2 from the antiferroelectric-to-ferroelectric phase demonstrated through polarization switching.

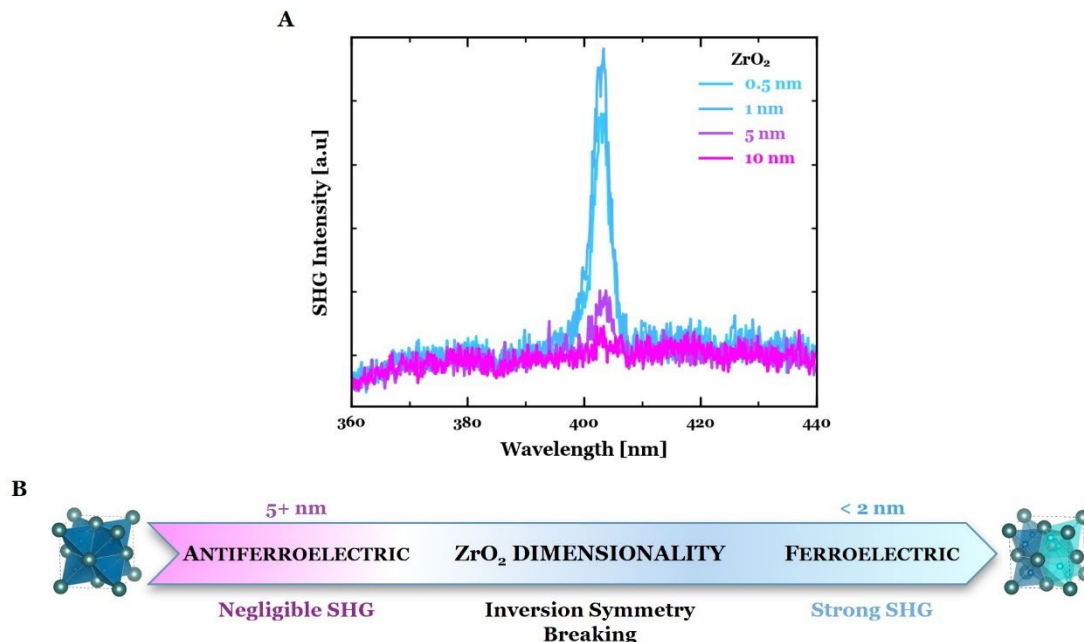


Fig. S11. Second harmonic generation (SHG) spectra. **(A)** SHG spectrum for ultrathin (0.5 nm, 1 nm) ferroelectric ZrO₂ films and relatively thick (5 nm, 10 nm) antiferroelectric ZrO₂ films, which demonstrate strong and negligible SHG intensity around 405 nm (810 nm fundamental laser beam), respectively, consistent with the SHG mapping trends (Fig. 2C). **(B)** Dimensionality-driven evolution of ZrO₂ from the nonpolar antiferroelectric phase to the polar ferroelectric phase indicated by inversion symmetry breaking.

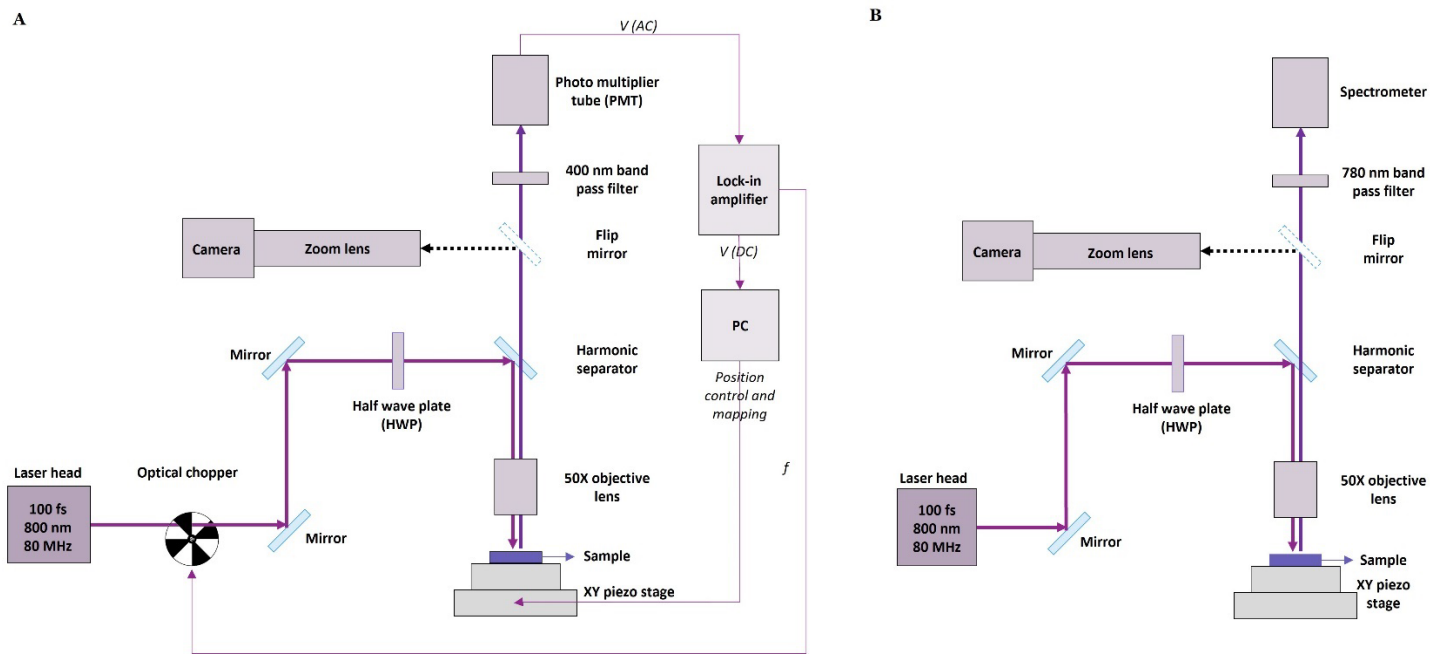


Fig. S12. Second harmonic generation (SHG) measurement setups. **(A, B)** Schematics for the spatially-resolved SHG (A, Fig. 2C) and emission spectrum SHG (B, fig. S11) setups used to probe in-plane symmetry breaking (Supplementary Text) in ZrO_2 films.

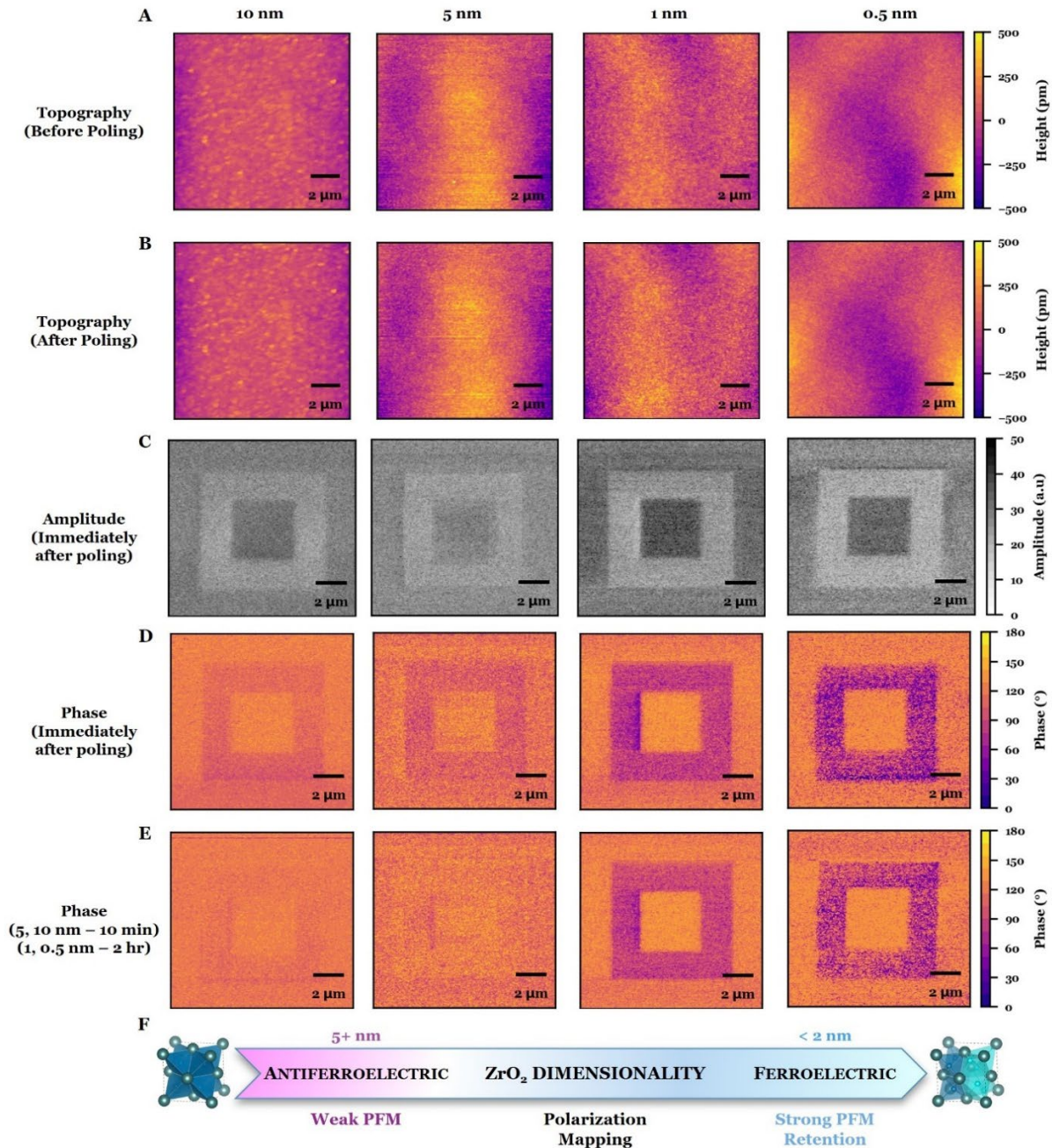


Fig. S13. Ferroic phase insights from scanning probe microscopy. (A, B) AFM topography before (A) and after (B) poling a box-in-box pattern onto ZrO₂ films of various thickness, demonstrating no topographic change to the ZrO₂ surface due to poling. The inner (outer) box was poled with positive (negative) bias. (C, D) PFM amplitude (C) and phase (D) images after poling a box-in-box pattern, demonstrating minimal contrast for relatively thick (5, 10 nm) ZrO₂ and strong contrast for ultrathin (0.5, 1 nm) ZrO₂. (E) Retention of PFM phase contrast. The weak contrast in relatively thick (5, 10 nm) ZrO₂ vanishes within 10 minutes; meanwhile, the strong contrast present in ultrathin (0.5, 1 nm) ZrO₂ remains after 2 hours, indicating long-term persistence of the ferroelectric polarization. (F) Dimensionality-driven antiferroelectric-to-ferroelectric evolution of ZrO₂ illustrated through polarization mapping.

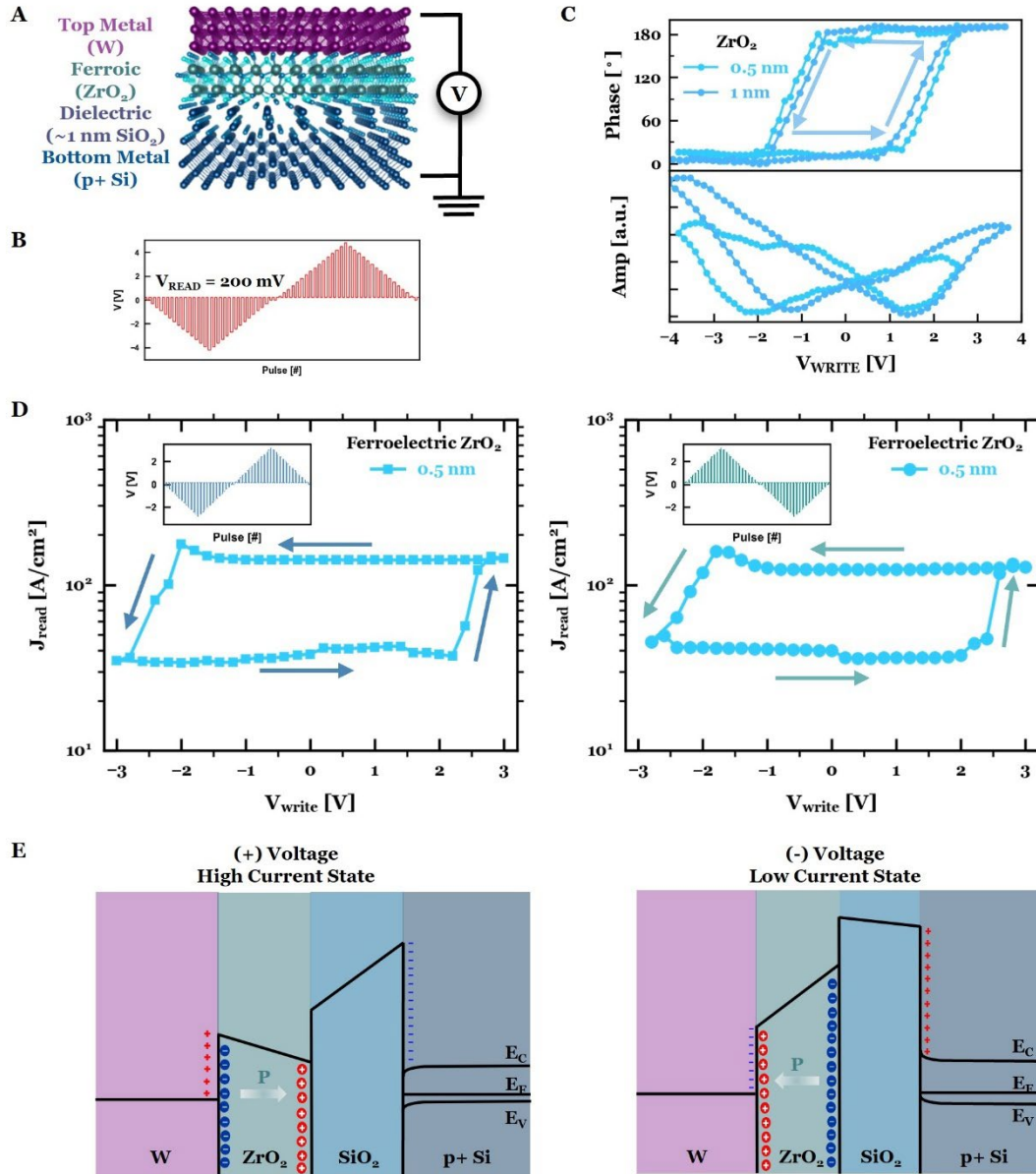


Fig. S14. Ferroic phase insights from field-dependent hysteretic measurements. **(A)** Schematic of metal-ferroic-insulator-semiconductor (MFIS) ferroic tunnel junction. **(B)** Voltage waveform used in pulsed I - V and PFM measurements. **(C)** PFM spectroscopy hysteresis loops for ultrathin (5 Å and 1 nm) ZrO₂; the 180° phase hysteretic behavior and butterfly-shaped amplitude loops are consistent with FE-like polarization switching. **(D)** Pulsed current-voltage (I - V_{write}) hysteresis map as a function of write voltage measured at 200 mV read voltage for ultrathin (5 Å) ZrO₂, consistent with FE-like polarization switching based on the counter-clockwise hysteresis sense **(E)**. The abrupt hysteretic behavior and saturating tunnelling electroresistance is characteristic of polarization-driven switching, as opposed to filamentary-based switching mediated by electrochemical migration (Supplementary Text). The ultrathin FTJ devices demonstrates voltage polarity-independent I - V_{write} hysteresis sense: both negative-positive-negative voltage polarity (left, blue) and positive-negative-positive voltage polarity (right, green) demonstrate counterclockwise hysteresis. The voltage polarity-dependent I - V hysteresis measurements further

rule out filamentary-based resistive switching mechanisms and is consistent with polarization-driven switching (Supplementary Text). Insets: Voltage waveform used in the pulsed $I-V_{write}$ measurements; the alternating sequence – staircase write, fixed read – mimics the PFM waveform. (E) Electronic band diagrams of the MFIS tunnel junction corresponding to the high-current (left) and low-current (right) states, depending on the remnant polarization in ZrO_2 . The high-current state (positive voltage applied to the W, ZrO_2 polarization points away from W) corresponds to a lower average tunneling barrier, and vice-versa for the low-current state. The uncircled '+' and '-' symbols in the metal and semiconductor represent holes and electrons, respectively, while the circled '+' and '-' symbols in the ferroic layer represent the dipole charges in the ferroic. In the band diagrams it is assumed that the ferroic bound charges at the metal/ferroic interface are perfectly screened and therefore the barrier height at the metal/ferroic interface is fixed and independent of polarization direction.

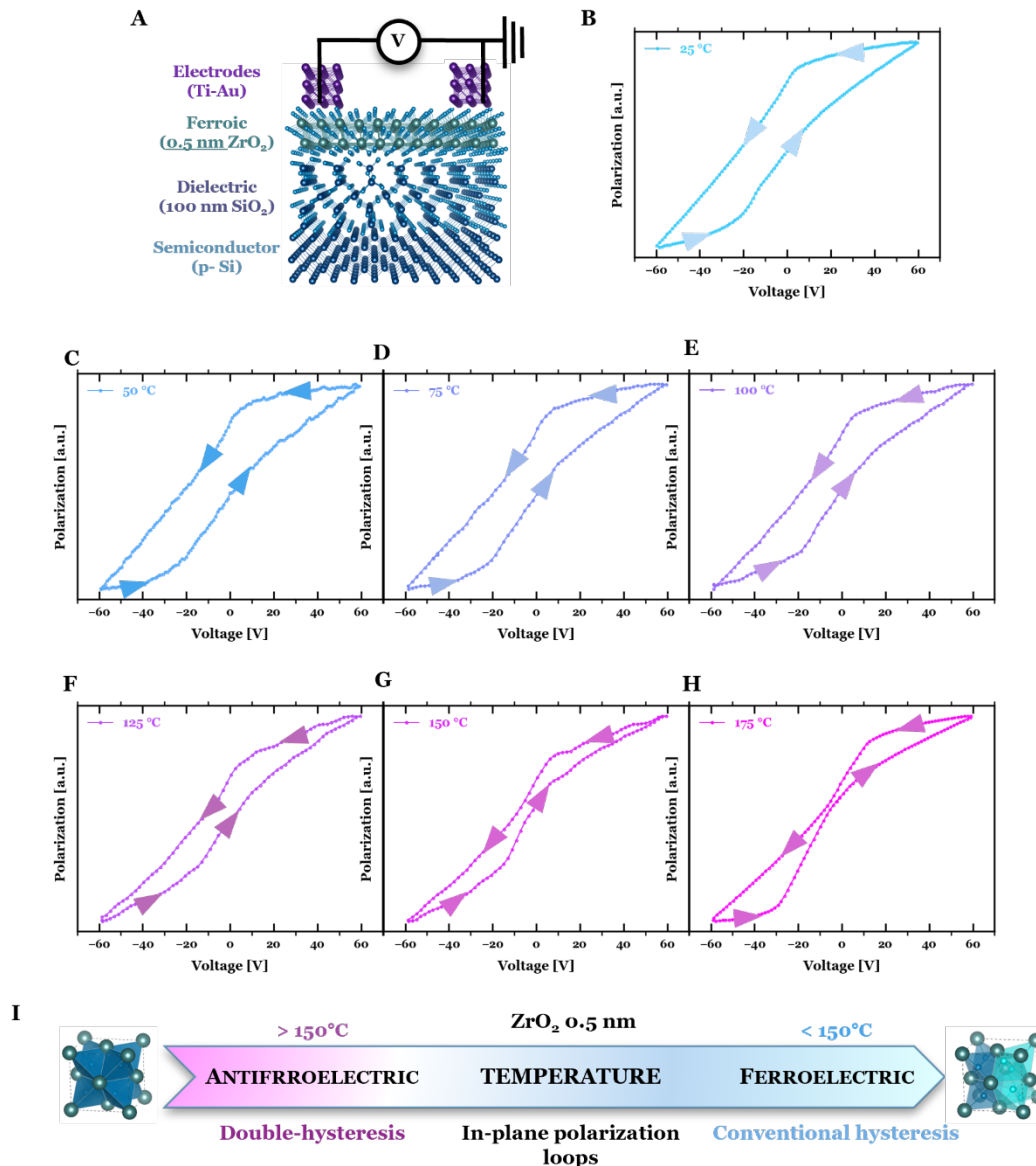


Fig. S15. Temperature-dependent ferroelectric-antiferroelectric phase transition in 0.5 nm ZrO_2 . (A) Schematic of the in-plane device structures used for temperature-dependent in-plane polarization-voltage (P - V) loops for 0.5 nm ZrO_2 films. (B,C,D,E,F,G,H) P - V loops from 25°C to 175°C in 25°C increments, starting with ferroelectric-like hysteresis at 25°C. The P - V loops become more pinched with increasing temperature until finally demonstrating complete antiferroelectric-like double hysteresis switching at 175°C. The Curie temperature is $\sim 150^\circ\text{C}$, well above room temperature. (I) Temperature-dependent antiferroelectric-to-ferroelectric phase evolution in 0.5 nm ZrO_2 demonstrated through polarization switching.